The Relationship Between Solar Radio and Hard X-ray Emission

S.M. White · A.O. Benz · S. Christe · F. Fárník · M.R. Kundu · G. Mann · Z. Ning · J.-P. Raulin · A.V.R. Silva-Válio · P. Saint-Hilaire · N. Vilmer · A. Warmuth

Abstract This review discusses the complementary relationship between radio and hard X-ray observations of the Sun using primarily results from the era of the *Reuven Ramaty High Energy Solar Spectroscopic Imager* satellite. A primary focus of joint radio and hard X-ray studies of solar flares uses observations of nonthermal gyrosynchrotron emission at radio

S.M. White (✉)
Space Vehicles Directorate, AFRL, Kirtland AFB, Albuquerque, NM 87123, USA
e-mail: Stephen.White@kirtland.af.mil

A.O. Benz
Institute of Astronomy, ETH Zürich, 8093 Zürich, Switzerland

S. Christe
NASA/Goddard Space Flight Center, Mail Code 671, Greenbelt, MD 20771, USA

F. Fárník
Astronomical Institute, Academy of Sciences, 251 65 Ondřejov, Czech Republic

S.M. White · M.R. Kundu
Dept. of Astronomy, University of Maryland, College Park, MD 20742, USA

G. Mann · A. Warmuth
Astrophysikalisches Institut Potsdam, An der Sternwarte 16, 14482 Potsdam, Germany

Z. Ning
Purple Mountain Observatory, Nanjing 210008, China

J.-P. Raulin · A.V.R. Silva-Válio
Centro de Radio Astronomia e Astrofisica Mackenzie, R. da Consolação 896, 01302-907 São Paulo, SP, Brazil

P. Saint-Hilaire
Space Sciences Laboratory, University of California, Berkeley, CA 94720, USA

N. Vilmer
Observatoire de Paris, LESIA—CNRS UMR 8109, 5 Place Jules Janssen, 92190 Meudon, France

Springer

wavelengths and bremsstrahlung hard X-rays to study the properties of electrons accelerated in the main flare site, since it is well established that these two emissions show very similar temporal behavior. A quantitative prescription is given for comparing the electron energy distributions derived separately from the two wavelength ranges: this is an important application with the potential for measuring the magnetic field strength in the flaring region, and reveals significant differences between the electrons in different energy ranges. Examples of the use of simultaneous data from the two wavelength ranges to derive physical conditions are then discussed, including the case of microflares, and the comparison of images at radio and hard X-ray wavelengths is presented. There have been puzzling results obtained from observations of solar flares at millimeter and submillimeter wavelengths, and the comparison of these results with corresponding hard X-ray data is presented. Finally, the review discusses the association of hard X-ray releases with radio emission at decimeter and meter wavelengths, which is dominated by plasma emission (at lower frequencies) and electron cyclotron maser emission (at higher frequencies), both coherent emission mechanisms that require small numbers of energetic electrons. These comparisons show broad general associations but detailed correspondence remains more elusive.

1 Introduction

From its earliest days, the study of hard X-ray emission from the Sun has had a natural ally in solar radio emission (Kundu 1961). The reason is straightforward: the electrons that produce hard X-ray emission have energies of order 10 keV or more, and such energetic electrons are also very efficient emitters of radio emission in the solar corona. That they can produce radio emission by a number of different physical mechanisms, in contrast to the bremsstrahlung-dominated hard X-rays, means that the radio data provide a range of diagnostics that complement the hard X-ray measurements. Between these two wavelength ranges we should expect to be sensitive to most sources of energetic electrons, both thermal and nonthermal, in the solar corona.

In this article we will review developments in our understanding of the joint use of radio and hard X-ray emission since the launch of the *Reuven Ramaty High Energy Solar Spectroscopic Imager* (*RHESSI*) satellite in 2002. In all cases discussed here, the hard X-ray emission most likely arises from bremsstrahlung emitted when energetic electrons are accelerated by Coulomb forces in collisions with ambient ions, either in the chromosphere or in the corona. Bremsstrahlung hard X-ray emission is proportional to the product of the nonthermal electron density and the ambient ion density. Inverse Compton emission is also a possible emission mechanism for the hard X-rays, but more extreme conditions are required and are not believed to be relevant for our discussion (e.g., see Krucker et al. 2008a). There are two general areas in which comparison of radio and hard X-ray (HXR) emission is relevant: phenomena (usually at higher radio frequencies, i.e., above 5 GHz) in which the radio emission is incoherent gyrosynchrotron emission[1], and those (usually at lower frequencies, i.e., below 2 GHz) where the radio emission is due to a coherent emission mechanism such as plasma emission or cyclotron maser.

---

[1]A note on terminology: it is conventional to reserve the term "synchrotron" for emission by highly relativistic electrons (Lorentz factor $\gamma \gg 1$) spiraling along magnetic field lines, while emission by mildly relativistic electrons is referred to as "gyrosynchrotron" in solar radiophysics.

2 Quantitative Comparison of Hard X-ray and Microwave Spectra

The study of radio emission from solar flares predates the detection of hard X-rays from the Sun, and the presence of activity at microwave frequencies in the impulsive phase of solar flares had been well established by 1958 when the first observation of a flare at hard X-ray/γ-ray wavelengths was carried out with a balloon-borne telescope over Cuba (Peterson and Winckler 1958). The authors of that paper noted the coincidence of the HXRs with microwave emission, and speculated that the "radio spectrum is emitted as betatron radiation from [electrons at energies of about 1 MeV] as they spiral in the intense magnetic fields associated with the sunspot group. These same electrons finally stop in the solar photosphere, where a small fraction of their energy is lost as bremsstrahlung γ-rays" (see also Kundu 1961). This remains our overall picture of the relationship between hard X-ray and microwave emission in the impulsive phase of flares: electrons with energies above 30 keV produce gyrosynchrotron radio emission as they spiral in ubiquitous magnetic fields in the corona, and bremsstrahlung HXRs when they precipitate into the dense chromosphere and lose their energy through collisions. The magnetic field strength B in the corona is typically of order 500 G over active regions, leading to electron gyrofrequencies ($2.8 \times 10^6 B$ Hz) of order 1–2 GHz in the low corona, and electrons with energies of order 100 keV and above radiate gyrosynchrotron emission at harmonics from the third upwards, usually dominating radio emission from flares at frequencies above 3 GHz. Typical flare radio spectra peak at 10 GHz (Guidice and Castelli 1975), although in larger flares the spectral peak can often occur at much higher frequencies.

In this picture we expect images of the radio emission at microwave frequencies to outline the field lines in the corona occupied by nonthermal electrons, while the HXRs show the same electron population as they strike the chromosphere at the footpoints of those field lines. With sufficiently good imaging, one could establish field-line connectivity by such a comparison. This picture can be distorted in several ways: the strength of the radio emission is proportional to a high power of B (e.g., Dulk and Marsh 1982) and thus electrons trapped in regions of strong magnetic fields will appear very bright, whereas strong magnetic fields near the surface tend to prevent precipitation of electrons with non-zero pitch angles due to magnetic mirroring and this effect could actually reduce gyrosynchrotron emission close to the footpoints compared to the rest of the loop.

Such comparisons of gyrosynchrotron and HXR emission remain a staple of high energy solar physics. One aspect to be borne in mind is that although radio telescopes are capable of excellent imaging and are generally more sensitive to nonthermal electrons than are HXR detectors, solar-dedicated radio telescopes capable of excellent imaging are few in number and it is difficult to arrange observations during flaring periods on non-solar-dedicated major facilities such as the Very Large Array (VLA). Therefore most of the radio work at microwave frequencies utilizes data from solar-dedicated arrays such as the Nobeyama Radio Heliograph (NoRH), the Owens Valley Solar Array (OVSA) or the Siberian Solar Radio Telescope.

We discuss the formalism for quantitative comparison of gyrosynchrotron radio data and bremsstrahlung hard X-ray measurements in the current section. Examples of scientific topics addressed specifically by comparison of *RHESSI* and microwave observations are given in the following sections.

2.1 Hard X-ray Bremsstrahlung Spectra

In the following discussion of HXR emission we follow the prescription of Hudson et al. (1978), based in turn on Brown (1971) and the Bethe-Heitler form for the bremsstrahlung

cross-section (see the discussion of cross-sections in Kontar et al. 2011). Essentially the same calculation was used by Nitta et al. (1991) and White et al. (2003) for quantitative comparison of radio- and HXR-emitting electrons. Assume that the hard X-ray photon spectrum is a power law of the form

$$\Phi(\epsilon) = A_0 \left(\frac{\epsilon}{E_0} \right)^{-\gamma} \text{ photons cm}^{-2}\,\text{s}^{-1}\,\text{keV}^{-1}, \tag{2.1}$$

where ϵ is the photon energy, γ is the power-law slope of the photon spectrum, and A_0 is the normalization constant at a fiducial photon energy E_0 keV. In the case of the widely-used OSPEX package of Richard Schwartz, $E_0 = 50$ keV is the default for the broken power-law fit to the spectrum and the normalization obtained from the fit refers to this energy. Given this photon spectrum, the corresponding electron flux energy spectrum into the target is given by

$$\frac{d^2\mathcal{N}(E)}{dE\,dt} = 3.28 \times 10^{33} \frac{A_0\,b(\gamma)}{E_{0,\text{keV}}} \left(\frac{E}{E_0} \right)^{-(\gamma+1)} \text{ electrons keV}^{-1}\,\text{s}^{-1} \tag{2.2}$$

(Hudson et al. 1978), where $b(\gamma) = \gamma^2\,(\gamma-1)^2\,B(\gamma-0.5, 1.5)$ and $B(x, y)$ is the beta function. The parameter $b(\gamma)$ is of order 10 to 60 for typical values of γ (3 to 6). The factor of E_0 appearing in the denominator here is in units of keV (per Brown 1971, p. 498, equation 15). We use $\mathcal{N}(E)$ to denote the total number of electrons at energy E in some volume: derivatives of this quantity with respect to volume and energy yield the volume number density and the energy distribution, respectively.

2.2 Thick-Target Hard X-rays

The electron flux into the HXR target cannot be compared directly with the microwave parameters since the relevant quantity for the radio emission is the total number of radiating electrons in the coronal volume, rather than a flux. Comparison of the two depends on the nature of the hard X-ray source. In this section we consider the so-called "thick-target" case, in which the radiating electrons immediately lose all their energy in a high-density source. The density of the source then does not appear in the formulae. To derive the nonthermal electron volume density from the energy distribution of the electron flux into the thick target, we assume the classic expression relating a density to a flux,

$$\frac{d^2\mathcal{N}(E)}{dE\,dt} = A_X\,v\,\frac{d^2\mathcal{N}(E)}{dE\,dV} \tag{2.3}$$

where A_X is the area of the X-ray source and v is the velocity of the electrons into the target. A_X must be obtained from observations, and its determination relies on high-quality imaging data.

The velocity v is treated as follows. For ultrarelativistic electrons it is assumed to be of order c with no energy dependence. For nonrelativistic electrons we assume, as an approximation, that the component of velocity into the target (i.e., the downwards component for thick-target emission from the chromosphere) carries one-third of the electron energy (equipartition between directions of motion). Thus we set

$$\frac{1}{2}mv^2 = \frac{1}{3}E \tag{2.4}$$

which leads to

$$v = c\sqrt{\frac{2}{3}\frac{E}{mc^2}} = 0.0361 E_{\text{keV}}^{0.5} c = 1.08 \times 10^9 E_{\text{keV}}^{0.5} \text{ cm s}^{-1}. \tag{2.5}$$

Substituting Eqs. 2.2 and 2.5 into Eq. 2.3, we find the following expression for the electron volume number density energy distribution in the nonrelativistic limit:

$$\frac{d^2\mathcal{N}(E)}{dE\,dV} = 3.04 \times 10^{24} \frac{A_0 b(\gamma)}{E_{0,\text{keV}}^{1.5} A_X} \left(\frac{E}{E_0}\right)^{-(\gamma+1.5)} \text{ electrons cm}^{-3} \text{ keV}^{-1}. \tag{2.6}$$

This formula indicates that for a given photon power-law index γ, the electron energy power-law index $\delta = \gamma + 1.5$ at nonrelativistic energies in a thick-target model, i.e., the energy spectrum of the electrons entering the target is actually steeper than the resulting thick-target bremsstrahlung photon spectrum. This occurs because the electron energy spectrum in the target is flatter than the injected energy spectrum, due to the fact that electrons with low energy lose their energy faster by collisions with ambient electrons, and thus are depleted in the target faster, than high-energy electrons.

The ultrarelativistic limit is somewhat complicated and simple expressions are not available. In terms of the spectrum, setting $v = c$ in Eq. 2.3 means that no additional power of E is added when the electron flux is converted to a number density, i.e., if this were the only change in the ultrarelativistic limit we would find $\frac{d^2\mathcal{N}(E)}{dE\,dV} \propto E^{-(\gamma+1)}$. In terms of the photon spectrum, this would actually imply that for a pure electron energy power law δ the bremsstrahlung photon spectrum would steepen in the ultrarelativistic limit compared to the nonrelativistic limit by 0.5 in the spectral index, i.e., $\gamma = \delta - 1$ instead of $\gamma = \delta - 1.5$. However, the electron-ion cross-section changes form in the ultrarelativistic limit, and electron-electron collisions play a more important role in producing bremsstrahlung at energies above the electron rest mass. Electron-electron bremsstrahlung results in a photon spectrum shallower by 1 in the spectral index than electron-ion bremsstrahlung (Vestrand 1988; Kontar et al. 2011). (The main energy loss of the incident electrons occurs in $e-e$ collisions, but at lower energies HXR photons are predominantly produced by the large deflections in $e-p$ collisions.) The combined result of all these effects seems to be to flatten the photon spectrum above 500 keV by about 0.5, i.e., $\gamma \approx \delta - 2$. McTiernan and Petrosian (1990) state that a rough integration of the product of electron flux and cross-section gives a flattening of the photon spectrum above 500 keV by $\log(E_\gamma/m_e c^2)$, although their calculation refers to fluxes rather than volume number densities. In any case, it does not seem to be readily feasible to derive quasi-analytical approximations in the relativistic limit: a crude approach is to join the nonrelativistic limit smoothly onto a power law 0.5 flatter above 500 keV.

2.3 Thin-Target Limit

In contrast to the thick-target limit, which is generally believed to apply to footpoint HXR sources, in the thin-target limit the electron energy distribution evolves only slowly under the influence of collisions. The rate of bremsstrahlung emission depends on the ambient ion number density n_i (cm^{-3}) in the source (assumed to be much larger than the density of any accelerated ions present). In this case, for a given photon spectrum (Eq. 2.1), we find that the nonthermal electron energy distribution is

$$\frac{d^2\mathcal{N}(E)}{dE\,dV} = 7.9 \times 10^{41} \frac{A_0 C(\gamma)}{n_i V_X E_{0,\text{keV}}^{0.5}} \left(\frac{E}{E_0}\right)^{-(\gamma-0.5)} \text{ electrons cm}^{-3} \text{ keV}^{-1}, \tag{2.7}$$

where $C(\gamma) = (\gamma - 1)/B(\gamma - 1, 0.5)$ and V_X is the physical volume of the hard X-ray source. In the thin-target limit, $\delta = \gamma - 0.5$, i.e., the electron energy distribution is flatter than the photon energy spectrum by about 0.5 in the index, whereas in the thick-target case the electron energy distribution is steeper than the observed photon energy spectrum.

2.4 Simplified Gyrosynchrotron Formulae

Exact calculations of the gyromagnetic emission by an energetic electron distribution are somewhat complicated and do not lend themselves to simple analytic formulae (e.g., Ramaty 1969; Takakura 1972). Faster numerical approaches have also been developed (e.g., Petrosian 1981; Klein 1987; Fleishman and Kuznetsov 2010). In order to have rough analytic estimates of the number density of the radio-emitting electrons, we use the Dulk and Marsh (1982) approximation formulae (see Dulk 1985, for corrected versions) for gyrosynchrotron emission. These describe a power-law distribution of mildly relativistic electrons, and are valid for isotropic electron pitch-angle distributions, harmonics in the range 20–100 and viewing angles (between the line of sight and the magnetic field direction) in the range 30°–80°. The physical property of the radio source that is easiest to measure and least dependent on a specific geometrical model is the brightness temperature at a point in the image, obtained at the highest frequency and spatial resolution possible. Other quantities, such as fluxes, require source areas to be known, and these are much more model-dependent than a localized brightness temperature. On the other hand, measuring the true brightness temperatures requires excellent high-spatial-resolution imaging. It is assumed that the radio spectral index α_r can be measured from two optically-thin frequencies (i.e., two frequencies above the flux peak in the radio spectrum). The expression for radio brightness temperature at a frequency f produced by an electron number density energy distribution

$$\frac{d^2\mathcal{N}(E)}{dE\,dV} = \mathcal{N}_r \, \frac{(\delta - 1)}{E_r} \left(\frac{E}{E_r} \right)^{-\delta} \text{ electrons cm}^{-3}\,\text{keV}^{-1} \qquad (2.8)$$

(here $\mathcal{N}_r$ is the number of electrons per unit volume in the distribution above the fiducial electron energy E_r, taken to be 10 keV by Dulk and Marsh 1982) in a magnetic field of strength B Gauss is

$$T_B = \kappa \, T_{eff} = 3.1 \times 10^{-0.53\delta} \, (\sin\theta)^{-0.45+0.66\delta} \left(\frac{f}{f_B} \right)^{-0.80-0.90\delta} \frac{\mathcal{N}_r L}{B}, \qquad (2.9)$$

where θ is the angle between the magnetic field and the line of sight, L is the line-of-sight depth through the source at the point where T_B is measured, and $f_B = 2.8 \times 10^6 \, B$ Hz is the electron gyrofrequency. Throughout this review we will use cgs units except for photon and electron energies, where in solar physics it is traditional to use keV rather than ergs as the energy unit.

Equation 2.9 results from multiplying together the Dulk (1985) expressions for opacity κ and effective temperature T_{eff}. We proceed to use Eq. 2.9 for T_B to determine the parameter $\mathcal{N}_r$ that appears in Eq. 2.8; note that $\mathcal{N}$ can also be derived directly from the X-ray Eq. 2.6 by equating it to Eq. 2.8, as presented below.

For convenience we write

$$\frac{f}{f_B} = \frac{10^9 f_{GHz}}{2.8 \times 10^6 \, B} = 357 \frac{f_{GHz}}{B} \qquad (2.10)$$

(where B is everywhere in units of Gauss) and find

$$T_B = 2.81 \times 10^{-2.00-2.83\delta} (\sin\theta)^{-0.45+0.66\delta} f_{GHz}^{-0.80-0.90\delta} \mathcal{N}_r \, L \, B^{-0.20+0.90\delta}. \qquad (2.11)$$

Inverting this expression to obtain $\mathcal{N}_r$ and substituting into Eq. 2.8 we find

$$\frac{d^2\mathcal{N}(E)}{dE\,dV} = 35.3 \, (\delta-1) \, 10^{3.83\delta-1} \frac{T_B}{L \, B^{-0.20+0.90\delta}} (\sin\theta)^{0.45-0.66\delta} f_{GHz}^{0.80+0.90\delta} E_{keV}^{-\delta}, \qquad (2.12)$$

in units of electrons $cm^{-3}\,keV^{-1}$. The quantity T_B can be measured directly if imaging observations of sufficient resolution are available; θ is usually assumed to be close to $90°$ since this maximizes the gyrosynchrotron emissivity; L can be estimated from the radio images; and since $\alpha_r = 1.20 - 0.90\delta$ is the radio flux spectral index, the value of δ obtained from the hard X-ray spectrum can be independently checked from the high frequency radio spectrum. The physical quantity in this equation that cannot be derived from observations is B, which appears as a very high power. In principle this too can be determined using the location of the radio peak frequency, which determines B via the following gyrosynchrotron approximation:

$$f_{peak} = 2.72 \times 10^{3.00+0.27\delta} (\sin\theta)^{0.41+0.03\delta} (\mathcal{N}_r \, L)^{0.32-0.03\delta} B^{0.68+0.03\delta}. \qquad (2.13)$$

A peak frequency of 10 GHz typically corresponds to $B \approx 600$ G (roughly the 6th harmonic of the gyrofrequency), with only a weak dependence on other physical parameters in the source (e.g., Dulk and Marsh 1982).

Equations 2.6 and 2.12 are two separate expressions for a volume density energy distribution and can be compared. When the spectral indices disagree by a large amount, as is often the case (with the energy distribution derived from radio data usually being flatter than that derived from HXR data), then it is usually assumed that they refer to different energy ranges: the optically-thin microwaves are more sensitive to electrons above 300 keV, while hard X-rays are usually dominated by electrons below 300 keV. This is illustrated in Fig. 1, which
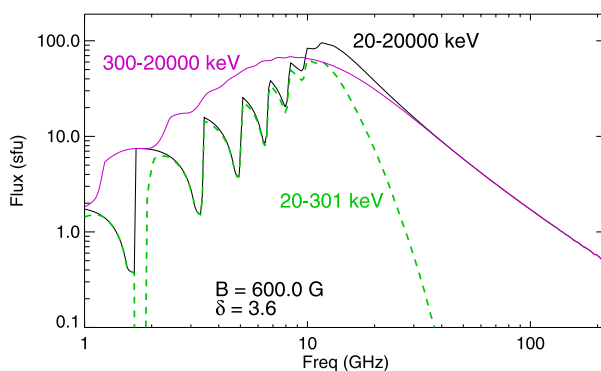

Fig. 1 A comparison of gyrosynchrotron radio spectra from electrons with different energy ranges. The *black line* is the spectrum produced by an electron energy power law from 20 to 20000 keV with a spectral index of 3.6 in a constant magnetic field of 600 G. The *green dashed line* is the spectrum produced by the lower-energy electrons from 20 to 300 keV, and the *purple dash-dot line* is the spectrum produced by the 300 to 20000 keV electrons. The calculation assumes a homogeneous loop of length $10''$, width $3''$ and depth $1''$, and an isotropic pitch-angle distribution for the radiating electrons. Radiative transfer is taken into account in the calculations

compares the gyrosynchrotron spectra of high- and low-energy electrons: electrons below 300 keV produce little radio emission above the spectral peak near 10 GHz (in the case of Fig. 1, at 30 GHz, the 20–300 keV emission is already two orders of magnitude weaker than the emission from the full energy range). When the electrons below 100 keV are present, they are sufficient to make the source optically thick at frequencies below the spectral peak, and the harmonic structure is clear (but will only be observed if the magnetic field is constant throughout the source, which is unlikely to be the case); when only electrons above 300 keV are present, they produce a smoother spectrum below the spectral peak because their harmonics are intrinsically broader. The spectrum shows some flattening above 40 GHz in the regime where relativistic particles dominate the emission. Note that the Dulk and Marsh formulae were derived from a full relativistic calculation for the gyrosynchrotron emission, so there is no contradiction in comparing the nonrelativistic thick-target bremsstrahlung results dominated by <500 keV electrons with the relativistic gyrosynchrotron emission dominated by >500 keV electrons, as long as the underlying electron energy spectrum has an unbroken power law (Eq. 2.2) from nonrelativistic to relativistic energies.

The discussion in this section relies on the paradigm that the nonthermal electrons are accelerated in the corona and then propagate down to the footpoints of the loops. Another complication for the comparison between radio and HXR results that needs to be borne in mind is that the number density appearing in Eq. 2.6 refers to the density entering the thick target at the footpoints, i.e., at some depth in the chromosphere depending on the electron energy (e.g., Brown et al. 2002), while the radio emission comes from the corona and the number density therefore refers to a different location in the loop. Implicit is also the assumption that the pitch-angle distribution is everywhere isotropic, corresponding to the fast pitch-angle scattering limit; an anisotropy in the pitch-angle distribution will affect the comparison (discussed further below).

2.5 Radio Flux from a Thick-Target Hard X-ray Spectrum

We may now derive an expression for the radio flux from an integrated hard X-ray spectrum under the thick-target assumption. Given the radio brightness temperature, in this case the Dulk and Marsh approximation (Eq. 2.9), we obtain the total radio flux from the standard expression (e.g., Dulk 1985, equation 14):

$$S = \frac{k_B f^2}{c^2} \int T_B \, d\Omega, \tag{2.14}$$

where the integral is over the solid angle Ω subtended by the radio source on the sky. We may replace the solid angle element $d\Omega$ with dA/D^2, where A is the actual physical area of the source on the sky and D is the distance of the source (in this case, D is one astronomical unit, 1.5×10^{13} cm). From Eq. 2.9 we may write

$$S = \frac{k_B f^2}{c^2} \int 2.81 \times 10^{-2.00-2.83\delta} (\sin\theta)^{-0.45+0.66\delta} f_{\text{GHz}}^{-0.80-0.90\delta} B^{-0.20+0.90\delta} \mathcal{N}_r \frac{L \, dA}{D^2}. \tag{2.15}$$

Now we note that $\int \mathcal{N}_r L \, dA$ is the integral of the number density per unit volume (above the reference energy E_r) over the volume of the source, i.e., it is the total number of electrons in the emitting volume, $\mathcal{N}_{tot}$. Combining the physical constants (note that one solar flux unit, or "sfu," is 10^{-19} ergs cm^{-2} s^{-1} Hz^{-1} in cgs units) and setting the angular factor to unity as an approximation (e.g., for $\theta = 70°$ and $\delta = 3.0$, $(\sin\theta)^{-0.45+0.66\delta} = 0.9$), we find

$$S_{sfu} = 1.9 \times 10^{-28.0-2.83\delta} \mathcal{N}_{tot} f_{\text{GHz}}^{1.20-0.90\delta} B^{-0.20+0.90\delta}. \tag{2.16}$$

2.6 The Effect of Anisotropy

The discussion presented above assumes an isotropic pitch-angle distribution for the radiating electrons. This is appropriate, e.g., when strong pitch-angle scattering in the flare loops, by collisions or by wave-particle interactions, isotropizes the particle distribution. This assumption is necessary to derive simple analytic formulae that can be applied (weak anisotropy is included in the papers by Petrosian 1982; Robinson 1985; Klein 1987), but may not be appropriate in many cases. Fleishman and Melnikov (2003a) discuss the effect of pitch-angle anisotropies on gyrosynchrotron emission in some detail. A single relativistic electron emits most of its radiation in a narrow cone around the direction of motion, but particles with small pitch angles barely radiate at all, so there can be large differences in the emission of electrons with large and small pitch angles. Tied to this question is the evolution of the pitch-angle distribution of a population of magnetically-trapped electrons both in time and in space. In a loop with significant variation in magnetic field strength between the footpoints and the loop top, conservation of the first adiabatic invariant means that the pitch angle of an electron will increase as it propagates towards stronger magnetic fields, and the electron will reflect at the height where its pitch angle reaches 90° ("magnetic mirroring"). Electrons with pitch angles sufficiently small for them to reach the solar chromosphere will "precipitate" (i.e., lose their energy immediately in collisions and stop) there and be lost from the corona. When gradual pitch-angle scattering takes place, without renewed injection of electrons, one ends up with a population of electrons with large pitch angles trapped near the loop top.

Fleishman and Melnikov (2003a) (with corrections in Fleishman and Melnikov 2003b) investigate changes to the gyrosynchrotron spectrum due to various forms of pitch-angle anisotropy at different observer viewing angles. Changes are more pronounced for viewing angles close to the magnetic field direction rather than perpendicular to the magnetic field direction in the source. The degree of polarization tends to increase as the anisotropy of the pitch-angle distribution strengthens, and the spectral index in the optically-thin limit is larger (steeper spectra) than for the isotropic pitch-angle distribution. In particular, loss-cone distributions viewed along the magnetic field show much weaker emission than isotropic distributions, and steeper high-frequency (i.e., optically thin) spectra: this can explain some observed differences between loop ends and loop tops for disk flares where the legs of the loop are viewed along the magnetic field and the loop top is viewed orthogonal to the magnetic field.

2.7 Transport Effects

Particle transport effects can also influence the appearance of microwave and hard X-ray sources, and delays between the two types of emission. Simultaneous imaging observations of radio and HXR sources can place physical constraints (loop lengths, source separations) on the flare site. We will not address these issues in detail here. We note that Melnikov et al. (2006) discuss the ways in which both pitch-angle distributions and particle transport effects can affect the microwave appearance of flaring loops. Minoshima et al. (2008) carry out detailed calculations of a trap-plus-precipitation model for a flare observed by *RHESSI* and NoRH. This flare exhibited HXR emission from two footpoints and a loop-top microwave source, and the authors argue that their model can explain the observation that the radio-emitting electrons appear to have a spectrum harder than that of the HXR-emitting electrons. As time proceeds, higher energy electrons will tend to concentrate in the trapped population of coronal loops, and this can explain observations such as the gradual hardening of the microwave spectrum even when the HXR spectrum is softening (e.g., Ning 2007, 2008a).

3 Thermal Bremsstrahlung Radio Emission from Flares

For completeness we include a brief discussion of thermal radio emission. The opacity due to bremsstrahlung of a uniform plasma of typical solar composition at temperature T_e and density n can be approximated by (e.g., Dulk 1985)

$$\kappa = 0.2 \frac{n^2}{T_e^{1.5} f^2} \text{ cm}^{-1}, \tag{3.1}$$

where n is measured in cm^{-3}, T_e in Kelvin and frequency f in Hz. From Eq. 2.14, the corresponding radio flux is given by

$$S = k_B/c^2 \Omega \begin{cases} T_e f^2 & \text{optically thick: } \kappa L \gg 1, \\ 0.2 n^2 L / T_e^{0.5} & \text{optically thin: } \kappa L \ll 1, \end{cases} \tag{3.2}$$

where L is the thickness of the source along the line of sight (in units of cm) and Ω is the projected solid angle on the sky occupied by the source. As above, the radio flux is traditionally quoted in units of sfu. As a crude rule of thumb, we may write Eq. 3.2 as

$$S = 2 \left(\frac{T_B}{10^6 \text{ K}} \right) \left(\frac{f}{10 \text{ GHz}} \right)^2 \left(\frac{r}{10''} \right)^2 \text{ sfu}, \tag{3.3}$$

where r is the radius of the area in which the brightness temperature is T_B (with $T_B = T_e$ in the optically-thick limit and $T_B = \kappa L T_e$ in the optically-thin limit).

Generally in solar flares, we find that the heated coronal plasma is optically thin to thermal bremsstrahlung above about 10 GHz, and this can be verified because, by Eq. 3.2, the flux spectrum should be almost independent of frequency (or equivalently, the brightness temperature spectrum, obtained from spatially-resolved images, varies as f^{-2}). A *GOES* class M1 flare typically produces a peak thermal flux of 1–5 sfu in the optically-thin flat-spectrum limit from the 10^7 K plasma to which *GOES* is sensitive, while an X1 flare produces of order 10–50 sfu of thermal emission. At low, optically thick, frequencies the spectrum rises as f^2. The $n^2/T^{0.5}$ dependence in the optically thin limit means that thermal bremsstrahlung is strongest in cool dense plasmas. In fact, if we take a given volume of optically thin plasma and heat it up without changing the density, the radio flux from the plasma will actually decrease due to the $T^{-1.5}$ dependence of the opacity. The *GOES* soft X-ray data are most sensitive to plasma at a temperature of order 10 MK, and if any cooler plasma is also present then the thermal radio emission will be larger than the flux level inferred from the *GOES* data alone. It should also be noted that the radio emission is produced by electrons whereas the soft X-ray emission has a large contribution from lines of highly-ionized atoms of elements heavier than hydrogen, so quantitative comparison of the two also depends on the abundance distribution of the radiating plasma (see the discussion in White et al. 2005).

4 Physical Properties of Flare-Accelerated Particles from Hard X-rays and Microwaves

As discussed in Sect. 2, if electrons with the same energy distribution produce both the microwave and hard X-ray emission from a solar flare, there should be straightforward relationships between the spectral indices of the two emissions. However, there has been a long

record of comparisons finding that in fact the radio and hard X-ray spectral indices are not compatible with the same electron energy distribution (e.g., Kundu et al. 1994; Silva et al. 2000). Since the typical (initial) energy of an electron emitting a HXR photon of energy ϵ is $1.5\epsilon - 3\epsilon$, with higher electron energies for flatter energy spectra (e.g., Kosugi et al. 1988; Aschwanden and Schwartz 1996), and microwave emission at higher frequencies is typically dominated by electrons with energies above 300 keV, it is desirable to have the hard X-ray spectral index at energies up to several hundred keV when making this comparison. Previously, such comparisons between microwave and HXR/γ-ray photon spectra up to several hundreds of keV have been possible with *GRANAT*/PHEBUS data (Trottet et al. 1998; Vilmer et al. 1999). Those studies found consistency between the spectral indices of the radio-emitting electrons and the HXR/γ-ray-emitting electrons at energies above several hundred keV.

4.1 SOL2002-07-23T00:35 (X4.8)

The first *RHESSI* flare for which this was possible was SOL2002-07-23T00:35 (X4.8). Before the main phase of this event, a remarkable distended precursor radio loop is seen, shown in Fig. 2 (Asai et al. 2006). The elongated loop structure is visible in both the 17 and 34 GHz images, extending over $80''$ to the north-east from the subsequent site of the flare (located at the base of this loop, marked in the middle panel of Fig. 2). In the 75 minutes for which NoRH images are available prior to the flare, the loop does not seem to change shape, nor are there significant changes in its brightness. On the other hand, the compact source at the base of the loop, which is not visible at 34 GHz and therefore may be nonthermal, declines steadily over this period until 00:18 UT, when pre-flare activity commences. EUV images of this region show no feature corresponding to the radio loop: it is difficult to measure its spectrum, but it may be thermal, suggesting that it is material much hotter than the $\sim 10^6$ K range to which the EUV images are sensitive.

Once the flare starts, intense nonthermal gyrosynchrotron emission from the main flare loops takes up the dynamic range of the images and the pre-flare loop is no longer visible. White et al. (2003) carried out a careful study of the main flare using radio imaging and spectral data from NoRH together with *RHESSI* data. In common with other large flares, this event had a high turnover frequency in its radio spectrum, necessitating the use of radio
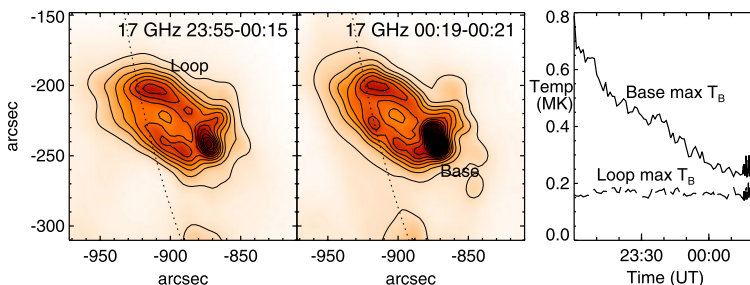

Fig. 2 The evolution of pre-flare emission at 17 GHz in SOL2002-07-23T00:35 (X4.8). The *left panel* shows an image averaged over the period 20 minutes prior to the impulsive phase, showing a distended loop with a compact source at its base. The *central panel* shows the image at 00:20 UT, with the source at the base brightening significantly. The contour interval is 2×10^4 K in both images. The *right panel* shows the light curves of the maximum 17 GHz brightness temperature in the compact source at the base (*solid curve*) and in the rest of the loop (*dashed line*)
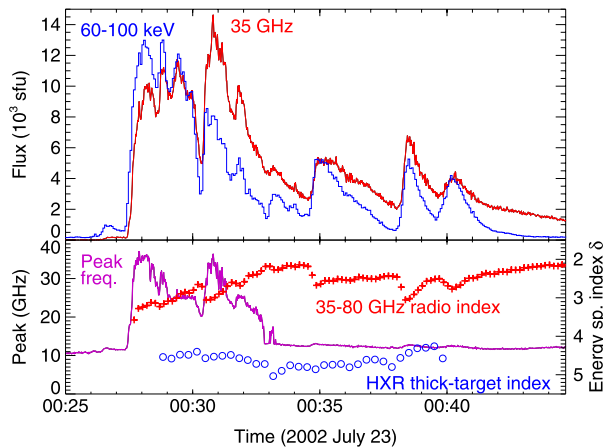
Fig. 3 Comparison (*upper panel*) of the *RHESSI* 60–100 keV hard X-ray light curve (*blue histogram*) and the NoRP 35 GHz light curve (*red solid curve*) for the well-observed flare SOL2002-07-23T00:35 (X4.8), as well as (*lower panel*) the time evolution of the radio spectral peak frequency (*purple solid line*) and the radio spectral index from 35 to 80 GHz converted to an electron energy spectral index assuming gyrosynchrotron emission from an optically-thin source (*red plus symbols*, uncertainty ±0.3). For comparison, the thick-target electron energy index obtained from the *RHESSI* 100–400 keV spectrum is also shown (*blue open circles*; formal uncertainty ±0.2). From White et al. (2003)

fluxes above 30 GHz in order to estimate the radio spectral index on the optically-thin high-frequency side. The imaging data were consistent with the picture in which the high-energy HXRs were emitted from the footpoints of coronal loops visible in the radio images.

Radio and HXR light curves for this event and the results of fits to the radio and HXR spectra are shown in Fig. 3. The structure of the 35 GHz light curve is representative of all radio frequencies above 4 GHz, and 60–100 keV is representative of the light curves for all hard X-rays above 30 keV; below 30 keV, the X-rays show less temporal fine structure in their light curves (Holman et al. 2003). The impulsive phase consists of a number of spikes and dips that are all seen in both the radio and HXR light curves. Different peaks have relatively different heights at the two wavelengths, but over the ∼20 minutes of the impulsive phase the similarity in time profiles is striking, including the brief sharp dip at 00:30:20 UT. Note that the rapid drop in radio emission exhibited during this dip implies that the trapping time for electrons in the corona must be very short (of order seconds) in this event.

The lower panel in Fig. 3 represents the spectral evolution of the radio emission using two parameters: the peak frequency (solid line), and the radio spectral index from 35 to 80 GHz (plus symbols), converted to the equivalent electron energy spectral index. The peak frequency in the spectrum, i.e., the frequency at which the radio flux is largest at any time, represents the boundary between the lower frequency emission from the regime where the source is optically thick and higher frequency emission from the regime where the source is optically thin. For comparison, the HXR spectral index from 100–400 keV, converted to an electron energy spectral index by assuming thick-target emission, is also plotted (as circles) in the lower panel, and it is clear that the two energy spectral indices are inconsistent with one another: as usual (e.g., Kundu et al. 1994; Silva et al. 2000), the radio data indicate a much flatter energy spectrum than do the HXR data.

Applying the quantitative analysis above to the hard X-ray data, we can estimate electron number densities in this event. The 40–400 keV photon energy spectrum at

00:35:00 UT, when the radio spectral peak is well below 34 GHz, has the form $9(E_\gamma/50 \text{ keV})^{-3.2}$ photons cm^{-2} keV^{-1} s^{-1}. The corresponding rate of electrons striking the chromosphere is $2 \times 10^{35}(E/20 \text{ keV})^{-4.2}$ electrons keV^{-1} s^{-1}. To convert this to a number density we need to divide by the electron speed v and the footpoint area A. The *RHESSI* images do not resolve the footpoints at a resolution of $7''$ and images made using grid 1 suggest a size as small as $2''$. If we adopt $A = 10^{16}$ cm^2, corresponding to a diameter of $2''$, using the formalism of the previous section we derive an energy distribution for the electron number density at the footpoints of 5×10^9 $(E/20 \text{ keV})^{-4.7}$ $(A/10^{16}$ cm$^2)$ electrons cm^{-3} keV^{-1}.

If we take the electron energy spectral index of 4.7 derived from HXR and apply it to the radio brightness temperature as discussed in the previous section, then the radio data also require very high densities.[2] Based on gyrosynchrotron theory, the brightness temperatures of over 10^9 K achieved at 17 GHz at the peak of the flare can only be produced by an electron energy spectrum as steep as 4.7 if the harmonic number is in excess of 30 (see figures in Dulk and Marsh 1982, confirmed by accurate numerical calculations). Such high harmonic numbers imply a relatively small magnetic field strength, no more than 200 G, and to achieve the same radio brightness temperature with the lower value of B, nonthermal densities over 10^{10} cm^{-3} above 20 keV are required, similar to those found above from the HXR data. The low value for B is consistent with the location of the brightest radio emission at the top of the arcade of loops. Caspi and Lin (2010) found that the superhot component in this flare (temperature of order 30–40 MK) required a magnetic field strength of at least 500 G to confine it, consistent with a picture in which the bulk of the nonthermal particles are located at a greater height than the superhot component. Even larger values of nonthermal electron density, with much stronger magnetic fields, were deduced by Raulin et al. (2004) in the case of SOL2001-08-25T16:45 (X5.3).

So, unfortunately, this extremely well observed event only adds to the problem of reconciling energy spectra derived from radio and HXR data. Since the radio and HXR profiles are so similar, we cannot argue that the radio emission comes from a long-lived population of trapped electrons while the hard X-rays come from directly precipitating electrons, as occurs in other events where the time profiles clearly differ (e.g., Raulin et al. 1999): the radio-emitting electrons have the same time behavior as the hard X-ray emitting electrons and should have a common origin and common evolution. There is a flattening in the *RHESSI* γ-ray spectra by about 0.5 in the index, but no sign in the data up to 8 MeV of the flattening by 2 implied by the radio data (Smith et al. 2003), so we argue that the radio spectral indices in Fig. 3 are not compatible with the *RHESSI* observations. We are forced to assume that the high-frequency radio emission is dominated by a region with a high turnover frequency so that the 35–80 GHz spectrum does not represent optically-thin emission, even in the later stages of the flare, and the true optically-thin radio spectral index is steeper than derived above. Nitta et al. (1991) reached a similar conclusion for their event. Both radio and HXR data require extreme number densities of nonthermal electrons to be accelerated in the energy release: over 10^{10} cm^{-3} above 20 keV. These numbers imply an acceleration mechanism of very high efficiency.

4.2 SOL2003-06-17T22:55 (M6.8)

Another well-observed flare is SOL2003-06-17T22:55 (M6.8) (Kundu et al. 2009). This flare is one of the few in which emission up to energies exceeding 200 keV can be imaged in

---

[2]Note that the fact that the energy spectral index derived from HXR is steeper than that derived from radio spectra implies that there are fewer high-energy electrons in the spectrum, and since these are the electrons that dominate the microwave emission, a larger total number of electrons is then required.
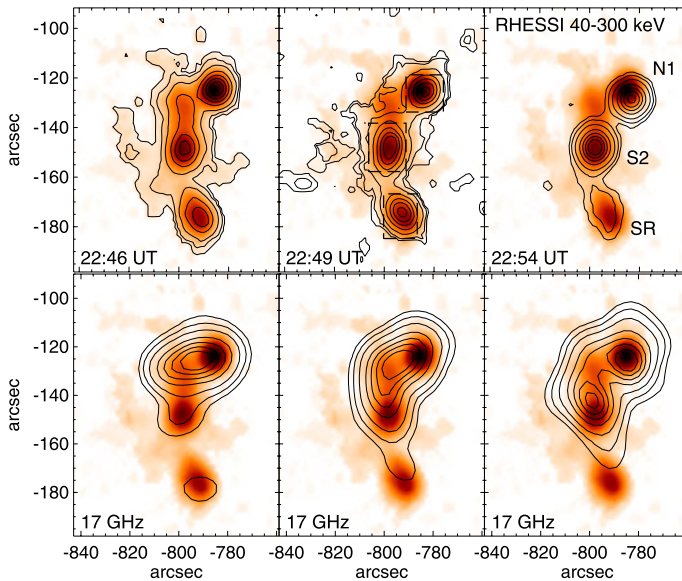
Fig. 4 *Upper panels*: hard X-ray images at each of the three main peaks in the HXR light curve (*contours*) of SOL2003-06-17T22:55 (M6.8). The images result from summing over the 40–300 keV range. The background image in each panel is the HXR image for 22:50 UT so that changes in morphology from one peak to the next can be seen. The resolution of the HXR images is 9″. The *middle panel* shows the regions used for the HXR spectra of sources S2, N1, and SR as *dotted boxes*. *Lower panels*: contours of simultaneous 17 GHz emission plotted over the HXR image of the flare from the *upper left panel*. Contours are at 4, 8, 16, 32, 48, 64, and 80% of the peak in each image. From Kundu et al. (2009)

hard X-rays, and we can investigate the HXR spectra of individual sources up to this energy. The morphology of the event is shown in Fig. 4. It takes the form of a filament eruption followed by a large double-ribbon flare with nonthermal emission stretching along a north-south axis over a neutral line. Three peaks each separated by about 5 minutes (times labeled in Fig. 4) are seen in the HXR light curve, and are matched in the radio data. In this case the radio and HXR morphologies are very similar, with both showing sources seeming to straddle the neutral line: the southernmost source is brightest during the first peak and then fades relative to the other peaks. Note that HXR and radio emission are both seen over a distance of more than 60 Mm along the neutral line in this one event: nonthermal energy release must have taken place throughout a large volume.

The distinctive feature of this event is that we can clearly separate three spatially distinct HXR sources during three different temporal peaks, and compare the energy spectra in each case. Figure 5 shows the *RHESSI* spectra for the three sources outlined by boxes in the upper middle panel of Fig. 4 during each of the three peaks, and Table 1 reports the spectral indices determined from power-law fits to these spectra (Kundu et al. 2009).

The fits to the spatially-resolved spectra assume a single power law over the 40–240 keV range, while the fits to the integrated spectra assume a broken power law over the range 50–400 keV. For peaks 1 and 2 the spectral break in the power law is above 200 keV and the fitted spectral index below 200 keV generally matches the fits to the spatially resolved spectra, which are dominated by photons below 120 keV, while the fit above the break gives a flatter spectrum. The uncertainties in the fits above the break are large due to the small number of high-energy photons detected, so one cannot conclude that there is flattening of
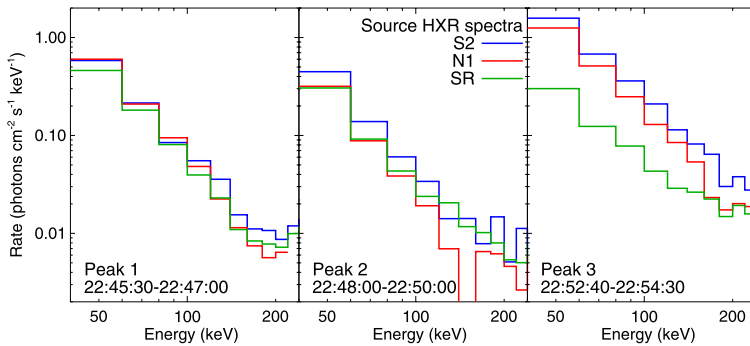
Fig. 5 Hard X-ray spectra at each of the three main peaks in the light curve for each of the three sources in the HXR images of SOL2003-06-17T22:55 (M6.8). These are derived from image cubes made in 20 keV channels from 40 to 300 keV. From Kundu et al. (2009)

Table 1 Power-law fits to the photon spectral index γ of individual sources in each of the three main peaks in the SOL2003-06-17T22:55 (M6.8) light curve derived from images in different energy bins, together with the fit to background-subtracted 50–400 keV spectra from the *RHESSI* front detectors. For the spatially-integrated spectra, the numbers are the results of a broken power-law fit: the spectral index at energies below the break, the break energy (keV) in parentheses, and the spectral index above the break. Uncertainties in the fits to the break energies are typically large (tens of keV)

Peak	S2 (middle)	N1 (north)	SR (south)	Spatially integrated
22:45:30–22:47:00 UT	3.1 ± 0.3	3.3 ± 0.3	3.0 ± 0.4	3.3 (280) 2.5 ± 0.2
22:48:00–22:50:00 UT	3.3 ± 0.1	3.5 ± 0.1	2.8 ± 0.5	3.4 (210) 2.0 ± 0.2
22:52:40–22:54:30 UT	2.7 ± 0.1	2.9 ± 0.2	2.1 ± 0.6	2.5 (120) 3.4 ± 0.2

the electron energy spectrum at high energies during the first two peaks (although note that fits to the *RHESSI* rear-detector spectra, more sensitive than the front detectors at high photon energies, agree with the results in Table 1 to within the uncertainties). We can also look at radio spectra for the individual peaks. NoRH images can be used to measure the spectral index for the three individual sources from 17 to 34 GHz, and again it is found that the inferred energy spectra are flatter than the energy spectra inferred from the HXR data with a difference in spectral index of order 1–2. Non-imaging data from the Nobeyama polarimeters (NoRP) up to 80 GHz suggest steeper radio spectra above 34 GHz, but there is a large uncertainty in the calibration of the NoRP 80 GHz data during this period and this leads to large uncertainties in the high-frequency spectral index. We do see significant anomalies between the radio and HXR properties of the sources: source SR is relatively bright at 34 GHz until late in the event, suggesting a very flat energy spectrum; the radio spectra do not show the same trend that all the spectra are flatter during peak 3. However, again we have major uncertainties in the location of the peak in the radio spectra of the individual sources since we only have images at two frequencies, and therefore we cannot determine whether the spectral index from 17 to 34 GHz actually represents the true optically-thin spectral index: if the 17 GHz source is partially optically thick then this frequency range will show a spectrum flatter than the true optically-thin spectral index. These problems again emphasize the need to have routine data at more than one frequency above 40 GHz if we are to be confident in measuring the true optically-thin radio spectral index in large flares.

The general conclusion of Fig. 5 and Table 1 is that a given peak shows the same energy spectrum (from HXRs) in all three spatial locations, but it may differ from one peak to the

next: peaks 1 and 2 clearly have steeper spectra than peak 3 (below 120 keV) in all three sources and in the integrated spectra. This suggests either that the electron acceleration mechanism has the same physical characteristics over a large spatial scale (5×10^4 km) or a more localized accelerator distributes electrons over the full volume. The challenge for the first interpretation is the fact that all sources show a flattening of their spectra in peak 3 after being steeper in peaks 1 and 2: how can sources so far apart have their characteristics change in the same way? For example, if acceleration is due to stochastic acceleration by wave turbulence, how is turbulence generated with identical properties over such a large volume? On the other hand, a localized accelerator that can distribute nonthermal electrons over a distance of 5×10^4 km is difficult to reconcile with the usual picture of post-flare loops in two-ribbon flares that are typically much shorter than the ribbons and straddle the neutral line rather than parallel the ribbons.

4.3 Coronal Hard X-ray Sources

The traditional picture of HXR arising from bremsstrahlung when nonthermal electrons strike the dense chromosphere is consistent with most observations. HXR sources in the corona are much less often observed, at least in part due to instrumental issues: imaging HXR telescopes typically have a limited dynamic range, and this limits their ability to see fainter thin-target emission from the low-density corona if it is competing with very bright thick-target footpoint emission from the high-density chromosphere. Coronal HXR emission is almost certainly present in most flares but difficult to observe, and a recent comprehensive review is devoted to this subject (see Krucker et al. 2008a).

There is one circumstance in which coronal emission does not have to compete with bright footpoint emission, and that is when the footpoints of flaring loops are obscured from our view by the solar limb. Such occulted flares have long been our main source of knowledge of coronal emission (e.g., Frost and Dennis 1971; McKenzie 1975; Kane et al. 1979), and this continues to be true in the *RHESSI* era. Krucker et al. (2010) observed a flare on 2007 December 31 that occurred 12° behind the limb as seen from Earth, but happily the event was within the field of view of telescopes on the *STEREO-B* spacecraft trailing the Earth in its orbit. *RHESSI* observed remarkably strong emission from this flare, up to 80 keV, despite the fact that the footpoints were occulted from *RHESSI*'s view. The 50 keV photon flux was comparable to what we see from the footpoints in a *GOES* class M flare.

In this flare (Fig. 6), the nonthermal HXR come from a source seen to lie at a height in the corona that is above the lower-energy thermal soft X-rays. This offset was seen previously in the famous "Masuda" flare (SOL1992-01-13T17:25, M2.0) (Masuda et al. 1994). NoRH images of the 2007 event show that the 17 GHz emission from the flare is co-spatial with the >30 keV source, but the larger occultation height at radio wavelengths (9 Mm above the optical limb) only allows us to observe the top part of the nonthermal HXR source at 17 GHz. The main flare loop seen during the soft X-ray peak time is occulted in the 17 GHz observations and emission from the initial source continues through the soft X-ray peak time. The microwave spectrum during the hard X-ray peak decreases with frequency as expected for gyrosynchroton emission and has a low turnover frequency, consistent with a coronal origin high above the solar surface. Based on the low turnover frequency of 2.5 GHz in the NoRP radio spectrum, the magnetic field strength in the 17 GHz source is estimated to be 30–50 G at a height 25 Mm above the solar photosphere. Since the electron gyrofrequency for this field strength is only 0.1 GHz, emission at 17 GHz is at harmonics in excess of 100 and requires relativistic electrons.
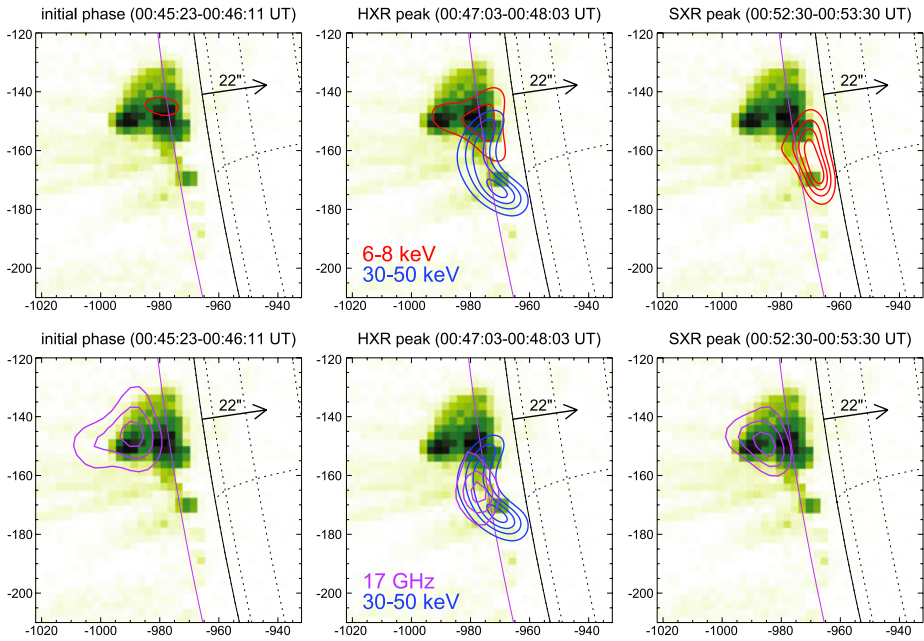
Fig. 6 X-ray and microwave imaging during the initial phase of SOL2007-12-31T01:11 (C8.3) (*left*), the hard X-ray peak (*middle*), and the soft X-ray peak (*right*). *Top row*: Contours in the thermal (6–8 keV, *red*) and the nonthermal (30–50 keV, *blue*) range are shown on an EIT 195 Å image taken towards the end of the main hard X-ray peak. The 6–8 keV contour levels are the same for all time intervals at 20, 40, 60, 80% of the maximum emission during the soft X-ray peak time, while the nonthermal emission is shown at 30, 50, 70, 90% levels. *Bottom row*: Microwave contours (*magenta*) at 17 GHz are shown at the 50, 70, 90% levels on the same EIT image. For comparison, the 30–50 keV source seen during the impulsive phase is shown as well (*blue*). The *magenta curve* gives the location of the limb at 17 GHz, about $12''$ above the photosphere; for this reason emission can be seen to lower heights in the HXR images than in the radio images. The *black arrows* indicate the occultation height for the flare location. From Krucker et al. (2010)

In this event the energy power-law spectral index of 3.4 derived from the radio data is not very different from the value of 3.7 derived from the *RHESSI* spectrum under the thin-target assumptions normally made for such coronal HXR sources. Because the occultation height for this event is so large and the ambient density in the corona is correspondingly low, extreme number densities of accelerated nonthermal electrons are required in order to explain the large HXR fluxes. No source of any kind is visible in the corona at the heights of the flare HXR emission prior to the event. From the absence of thermal HXR emission at the site of the harder photons during the flare, an upper limit of 8×10^9 cm^{-3} can be placed on the ambient density. The observed HXR flux at 50 keV then requires a density for the nonthermal electrons above 16 keV in excess of 10^9 cm^{-3}; for a more plausible ambient density of 2×10^9 cm^{-3} at a height of 16 Mm above the photosphere, the nonthermal electrons would have to outnumber the ambient ions in order to explain the observed HXR fluxes.

Thus in this event the standard electron-beam scenario where suprathermal electrons move through an ambient plasma producing hard X-ray emission by bremsstrahlung does not work. The main problems are that the number of accelerated electrons is comparable to the total number of electrons in the pre-flare source and that collisional heating would increase the ambient plasma temperature to superhot temperatures within seconds, producing

a bright thermal HXR source. Since no such source is seen, this picture cannot be correct. Rather, the nonthermal HXR source seems to be produced by a mechanism that accelerates all electrons and produces an entirely nonthermal electron distribution. This suggests that the above-the-looptop source is the acceleration region itself. In a purely nonthermal electron distribution, collisional losses to electrons are much reduced, making it an efficient hard X-ray source. Once a significant fraction of the electrons is accelerated, collisional losses of an accelerated electron are reduced due to a smaller number of ambient electrons. This simple picture suggests that once a significant fraction of electrons is accelerated, it might not take that much more to accelerate all of the electrons. Observations of a similar event in which the pre-flare density in the region of the nonthermal HXR source can be measured are needed to confirm this picture.

Asai et al. (2007) also report joint *RHESSI* and NoRH observations of an over-the limb M4 flare (SOL2005-07-27T05:02) whose footpoints were occulted in HXR. In that event, a filament eruption preceded the flare and was clearly visible in the NoRH 34 GHz images; again, nonthermal coronal sources are seen in both 25–40 keV HXR and in the microwave data, but in this event the energy spectra inferred from the two wavelength ranges differ greatly. The radio spectrum in this event has a spectral peak near 10 GHz, i.e., much higher than in the Krucker et al. (2010) event, suggesting that effectively none of the radio emission is obscured from us.

In the Krucker et al. (2010) event, the radio-deduced and HXR-deduced electron energy spectra are compatible with one another. It is evident that the discrepancy between the energy spectral indices derived from the microwave and HXR data in events such as SOL2002-07-23T00:35 (X4.8) and SOL2003-06-17T22:55 (M6.8) would be largely removed if the appropriate comparison were with thin-target bremsstrahlung rather than thick-target: as noted earlier, the actual energy spectrum of electrons in a thick-target HXR source is flatter than the injected spectrum due to the faster energy loss rate of lower-energy electrons. For the thick-target spectrum to be the appropriate comparison, the radio emission from the flare would have to be dominated by the electrons in the HXR source. In active regions where flares occur, the filling factor of strong magnetic fields at the surface is high and there is little if any difference between the field strength in the upper chromosphere and that in the lower corona. Therefore, since the volume of the footpoint thick-target HXR sources is so much smaller than the volume of the coronal loop that connects the footpoints (the footpoint sources have a depth typically less than $1''$ at the top of the chromosphere, whereas a coronal loop can be $20''$ long), and the incident nonthermal density at the footpoints will be smaller than the average nonthermal density in the loop if there is any magnetic mirroring, the only way that the electrons in the thick target can dominate the radio emission is if there are no nonthermal electrons in the coronal loop, i.e., the nonthermal electrons are entirely confined to the chromosphere. Images of disk flares such as Fig. 4 may seem to suggest that the locations of the radio emission are consistent with the HXR footpoints, but such images can be misleading due to their limited spatial resolution: loops smaller than the resolution of the radio images cannot be identified as loops in such images, and the distinction between footpoint sources and loop emission cannot be made. In general (see Sect. 5), radio images of flares are consistent with the paradigm that the radio emission is dominated by coronal sources. In any model in which the electrons are accelerated in the corona, there must always be many more electrons in the coronal volume than in the small volume occupied by the bremsstrahlung-emitting electrons in the narrow layer of the chromosphere at the footpoints of the coronal loop. In this case it remains appropriate to use the thick-target determination of electron energy spectra described in Sect. 2 for comparison with the spectral index determined from gyrosynchrotron observations.

4.4 Oscillations

Any periodic or quasi-periodic behavior observed in flares is valuable because it can reveal the characteristic frequency of a physical process or environmental property and thus has diagnostic value. There have been a number of events in which such periodicity has been seen simultaneously in microwaves and hard X-rays, confirming a common origin for the electrons radiating in the two wavelength domains and providing strong constraints on the physical processes involved (e.g., Nakajima et al. 1983; Asai et al. 2001; Grechnev et al. 2003). Fleishman et al. (2008) discuss another event in which oscillations are seen both in microwave data from the Owens Valley Radio Observatory and the Nobeyama Radioheliograph, as well as in the *RHESSI* hard X-ray light curves. Periodicities in the range 15–20 s are found in both wavelength ranges, with degrees of modulation typically around 10% or lower; at radio wavelengths, the degree of modulation rises with frequency, suggesting that it is larger in the optically-thin regime and thus that it is the number density of nonthermal electrons that is being modulated. They also find that the modulations at lower radio frequencies lead the higher frequencies in time by a small amount, and that modulation of the circular polarization is in the opposite sense to the modulation of the intensity: circular polarization is weakest when the intensity is strongest.

Another event exhibiting modulations simultaneous in HXRs and radio is SOL2003-11-03T09:55 (X3.9) (Dauphin et al. 2005). In this event, the later phase of HXR emission shows a quasi-periodic train of peaks with a period of order 35 s. These peaks are clear both in the 150–300 keV HXR light curve and in the microwave light curves. Surprisingly, the decimetric emission at 432 and 327 MHz shows the same modulations. Images from the Nançay Radio Heliograph at 432 MHz during the modulations show three different sources: one close to the limb, just above the HXR source locations in *RHESSI* images, and two other sources several hundred arcsec higher in the corona. The higher 432 MHz sources show more pronounced modulations than the lower source, despite being further from the modulated HXR footpoint sources. The correlation of the decimetric emission with microwaves and HXRs suggests that the emission mechanism is still gyrosynchrotron emission at decimetric wavelengths. Since the Razin effect is usually thought to suppress gyrosynchrotron emission at such low frequencies, this observation suggests that Razin suppression is not effective in this event, at least for the higher sources, and further that the gyrosynchrotron-emitting nonthermal electrons have access to large loops at the height of the 432 MHz sources. (Note that this event was also remarkable for the fact that it exhibited a Type II radio burst from a shock apparently driven by soft X-ray loops rising rapidly into the corona; see Dauphin et al. (2006).)

Possible interpretations of such oscillations have been reviewed by Nakariakov and Verwichte (2005) and Nakariakov and Melnikov (2006). Fleishman et al. (2008) test two models with their event: oscillations driven by MHD loop oscillations, or quasi-periodic injections of fresh nonthermal electrons into a stable source. An important constraint is that the oscillations are observed to be essentially in phase across the whole microwave spectrum, whereas a number of MHD modes (sausage, torsional) would predict that the optically thick (lower) frequencies and optically thin (higher) frequencies should show opposite behavior. Thus, the authors conclude that quasi-periodic injections of fresh nonthermal electrons provide a better fit to the observations.

4.5 Microflares

This topic is discussed at greater length by Hannah et al. (2011) and here we briefly mention radio aspects of HXR microflares. Kundu et al. (2006) compared the radio and HXR emis-

sion in a sample of microflares, using *RHESSI* and NoRH data. Microflares, X-ray bright-point flares, coronal X-ray jets and active region transient brightenings are all consequences of energy releases in the corona that are smaller than traditional flares, but are nonetheless clearly identifiable phenomena. The sample of 30 microflares studied by Kundu et al. (2006) showed relatively soft (i.e., steep) HXR spectra, which would lead one to expect that they would not possess sufficient mildly relativistic nonthermal electrons radiate strongly at microwave frequencies. Yet most of the microflares exhibit nonthermal microwave emission that requires electrons with energies exceeding 100 keV. This suggests that the radio-emitting electrons must have a harder energy spectrum than the HXR-emitting electrons: the imaging results show that typically the radio and HXR emission are not exactly coincident, supporting the possibility that the two electron populations are different. On the other hand, Ning (2008b) investigates a sample of apparently radio-quiet microflares and finds that their HXR properties are normal for microflares, as in the sample of Kundu et al. (2006). Ning (2008b) used less sensitive microwave patrol data for the microwave fluxes, and it is possible that more sensitive NoRH observations would have detected nonthermal radio emission.

A prior study by Qiu et al. (2004) investigated somewhat larger events (up to *GOES* B2 in soft X-ray class) using *RHESSI* and OVSA data. The advantage of OVSA data is that complete radio spectral information is available, but their detection level of around 1 sfu is not capable of addressing events weaker in the radio domain. About 40% of their sample of about 200 events are detected in microwaves, with emission up to about 10 GHz and spectral peaks in the 5–10 GHz range: thus their microwave spectra behave like standard nonthermal gyrosynchrotron spectra and strongly resemble those of normal flares. Where measured, the radio spectra typically suggest harder electron energy distributions than the HXR spectra exhibit, and some microflares with negligible responses in the *GOES* soft X-ray range nonetheless can have strong nonthermal microwave emission, emphasizing again the possible differences between the lower-energy nonthermal electrons to which HXRs below 25 keV are sensitive, and the higher-energy electrons responsible for the microwave emission.

5 Morphological Comparison of Microwaves and Hard X-rays

As noted earlier, we have the expectation that radio images will illuminate the paths of nonthermal electrons along magnetic loops in the corona whose footpoints are outlined in HXR by precipitating nonthermal electrons. We have to bear in mind the differences in HXR and radio imaging data: the best *RHESSI* images have a dynamic range of order 100, whereas radio images (e.g., from NoRH and the VLA) can achieve a dynamic range of order 10^4, and thus the radio images can show secondary sources in locations where the *RHESSI* images do not have enough dynamic range for sources to be visible above the noise. On the other hand, the brightness of the radio emission is strongly weighted by magnetic field strength, and this can lead to different emphases in the images at the two wavelengths.

5.1 "Loop" Flares

We expect radio images of flares to outline magnetic field lines carrying trapped energetic particles: any such particles on open field lines rapidly move out into the solar wind (it takes 5 seconds for an electron at speed $0.5c$ to propagate to 1 R$_\odot$) and are not present in the regions of strong magnetic fields low in the Sun's atmosphere long enough to contribute significantly to the microwave emission (but they may be seen via their plasma emission as
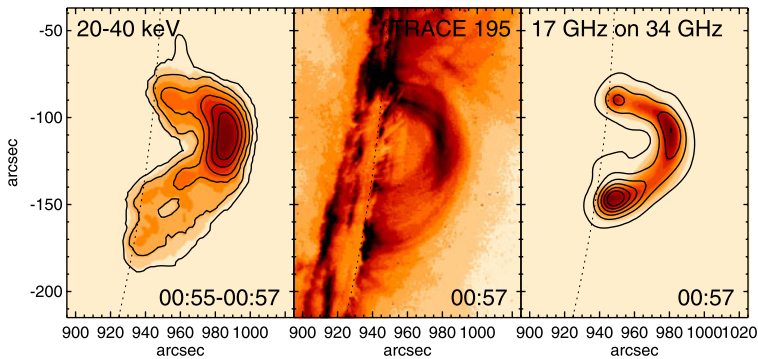
Fig. 7 Images of the early phase of the loop flare SOL2002-08-24T01:12 (X3.1) on the west limb. The *left panel* shows the *RHESSI* image of nonthermal 20–40 keV HXR photons covering the period 00:55–00:57 UT. The *middle panel* shows a *TRACE* 195 Å image at 00:57 UT, while the *right panel* shows contours of the emission at 17 GHz overlaid on a color image of the 34 GHz emission, also at 00:57 UT. Contours in the HXR and radio images are at 5, 20, 35, 50, 65 & 80% of the maximum in each image. The placement of the *TRACE* image relative to the other wavelengths is uncertain

Type III bursts instead). In fact, flare radio images that clearly look like magnetic loops are the exception, not the rule. This may be partly due to limited spatial resolution: since NoRH has a typical resolution of order $10''$, any loop needs to be quite large to appear as such in the radio images. Another factor is that the magnetic field variation along a loop can emphasize emission from strong-field regions or regions with $\theta \approx 90°$ so much that a loop morphology is not evident. Accordingly, events that do have a loop-like morphology tend to be heavily analyzed.

By far the favorite loop event for radio studies during the *RHESSI* period is SOL2002-08-24T01:12 (X3.1) on the west limb (Karlický 2004; Li and Gan 2005; Melnikov 2006; Tzatzakis et al. 2008; Romano et al. 2009; Reznikova et al. 2009; Ning and Cao 2009), which also produced a fast (1900 km s^{-1}) CME and an energetic particle event at the Earth. Figure 7 shows images in HXRs, microwaves and the EUV 195 Å band (Fe XII and Fe XXIV) during the early part of the impulsive phase, for which *RHESSI* data are available. The apparent loop has a footpoint separation of order $70''$ and height of order $50''$. The images provide an interesting contrast: in HXRs at tens of keV, presumably from nonthermal electrons, we see a pronounced brightening at the top of the "loop" in this early stage of the flare (here we use quotation marks to emphasize to the reader that while the source appears from our line of sight to be a "single loop"; in fact it could equally well be an arcade of loops extended significantly east-west, but co-located in projection along our line of sight). Line-of-sight effects can also play an important role in the appearance of the radio source, as discussed in Sect. 2. The flare apparently occurred on the visible disk and hence footpoint HXR sources should be visible, but they are not pronounced in these images; there is some evidence for multiple sources in the region of the southern footpoint at times before 00:55 UT. The radio images also show a bright peak at the top of the loop, but at 17 GHz the brightest source is at the southern footpoint, in a region that appears extended along the limb in the HXR images. The EUV image shows dense cool (Fe XII) and hot (Fe XXIV) material, the latter also detectable by *RHESSI* via its observations of the Fe and Fe–Ni X-ray emission-line complexes (Caspi et al. 2010).

The radio light curve for this event shows a number of intensive peaks over a period of 10 minutes starting at 01:00 UT, requiring repeated injections of energetic particles onto
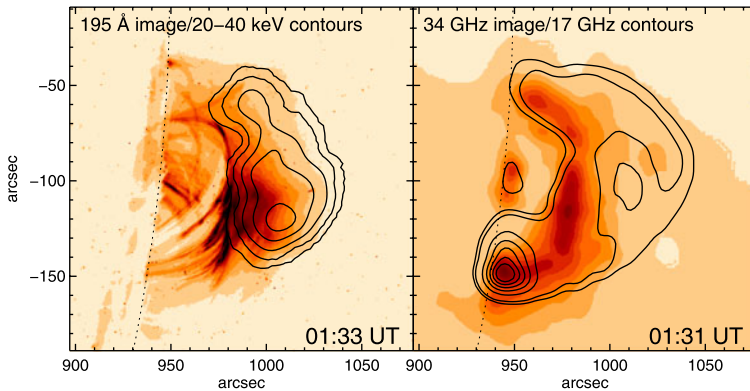
Fig. 8 Images of SOL2002-08-24T01:12 later in the event during the extended gradual phase (near 01:30 UT). At this time the 17 GHz image (contours at 4, 6.5, 20, 35, . . . , 80% of the maximum, *right hand panel*) shows two loops as well as a bright source at the southern footpoint, while the 34 GHz image (underlying image in *right hand panel*) only shows the lower loop and a (relatively) much weaker southern footpoint source. The *RHESSI* 20–40 keV image of nonthermal HXR (contours at 10, 30, 50, 70, 90% of maximum, *left panel*) only shows a high coronal source, roughly filling the region between the two loops in the 17 GHz image, and lying above the cooler (2 MK) loops visible in the TRACE 195 Å Fe XII image (*left panel*, image). The 2 MK loops appear to occupy a smaller volume than the 17 GHz radio source

the coronal loops. Reznikova et al. (2009) analyzed the evolution of the radio morphology and found that each peak showed the same behavior: during the rise of a peak the southern footpoint is brightest at 17 GHz, but as each peak decays the loop top starts to dominate the images. Reznikova et al. (2009) interpret this as requiring that the highest density of nonthermal electrons always be located at the loop-top where the magnetic field is weakest, while the nonthermal density in the footpoints is initially high but decreases with time. An implication of this interpretation is that pitch-angle scattering must always be weak in the radio-bright region at the loop top. The question arises as to whether these injections occur onto increasingly higher field lines, as in the helmet-streamer reconnection scenario, or onto essentially the same field lines, as expected for a confined flare. Li and Gan (2005) measured the radius of a circular fit to the radio "loop" at 34 GHz and found that the radius of the loop shrank steadily until 01:02 UT, and increased thereafter.

Later in the flare (01:30 UT; see Fig. 8) the 17 GHz radio images show two loops well separated in height, while the 34 GHz images only seem to show the lower loop. The brightness temperature of the lower loop is 2–3 MK at 17 GHz and around 0.6 MK at 34 GHz, while the upper loop has a 17 GHz brightness temperature of 1–2 MK but is less than 0.05 MK at 34 GHz. The radio spectrum of the lower-altitude loop is consistent with thermal emission from a post-flare arcade of loops. Karlický (2004) argues that the higher loop, with its nonthermal radio spectrum, is emitting by gyrosynchrotron emission and its appearance requires ongoing acceleration of electrons to nonthermal energies in the extended phase of the flare. The presence of a very bright source at the southern footpoint, with brightness temperatures (over 20 MK at 17 GHz, less than 0.6 MK at 34 GHz) indicating nonthermal emission, supports this argument, as does the presence of significant emission in the 20–40 keV range in the same volume as the nonthermal radio emission (Fig. 8, left panel).

Loop morphologies can also show up in thermal emission. Bone et al. (2007) discuss the development of a bright compact loop which has a flat radio flux spectrum and thus appears to be radiating by thermal bremsstrahlung. Densities of close to 10^{11} cm^{-3} are inferred. Another flare occurs in the same set of loops 30 minutes later, and Veronig and Brown
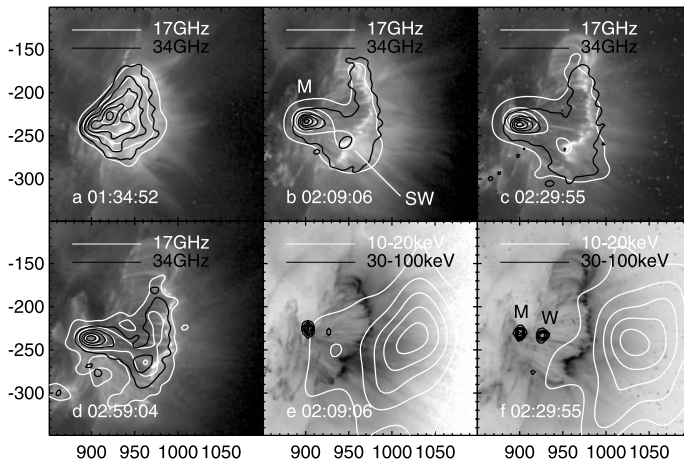
Fig. 9 The evolution of the radio and hard X-ray sources later in SOL2002-08-24T01:12 (X3.1). The first four images show a sequence of overlays of 17 GHz (*white contours*) and 34 GHz (*black contours*) images on *TRACE* 195 Å FeXII/FeXXIV images during the extended phase of the flare when the loop system is expanding above the west limb. The upper four contour levels are at 30, 50, 70 & 90% of the maximum in each image, while the lowest contours are at 10, 4, 2 & 1%, respectively, to match the changes in the peak intensity. *RHESSI* observes the early impulsive phase of the event and then goes into eclipse until 02:08 UT, and the last two images show contours of the *RHESSI* 10–20 keV (*white*) and 30–100 keV (*black*) emission overlaid on the *TRACE* 195 Å FeXII/FeXXIV images at 02:09:56 UT and 02:29:55 UT (displayed with inverted color table). The prominent nonthermal radio source is visible at the eastern base of the radio emission from 02:00 UT onwards. The radio emission from the loop tops at the northern end of the arcade has a flat spectrum and hence is probably thermal free-free emission. The 10–20 keV hard X-rays originate above the EUV loops, in higher soft X-ray emitting loops, while the harder 30–100 keV X-rays originate at the same location as the nonthermal radio source. From Kundu et al. (2004)

(2005), from analysis of the *RHESSI* hard X-ray spectra, inferred that the flare must have occurred in a very dense environment. The subsequent analysis of the radio data by Bone et al. (2007) confirmed this conclusion. Further discussion of this topic may be found in the chapter by Fletcher et al. (2011).

5.2 SOL2002-04-21T01:51 (X1.5)

The well-studied limb flare SOL2002-04-21T01:51 (X1.5) exhibited a spectacular arcade of post-flare loops in EUV images. Kundu et al. (2004) studied the radio emission from this flare and found, much as in SOL2002-08-24T01:12 (X3.1), that bright nonthermal sources were seen at a number of locations low in the corona, while the top of the post-flare arcade clearly shows thermal bremsstrahlung emission from the dense plasma there. Distinct regions of radio emission with very different time behavior can be identified in the radio images, and in particular a peculiar nonthermal source seen in radio and hard X-rays low in the corona at the base of the arcade is seen to turn on at 01:45 UT, some 30 minutes after the start of the impulsive phase (Fig. 9).

This event is striking for the wide range of types and locations of both radio and hard X-ray emission it displays. The energy distribution inferred for the radio-emitting electrons during the impulsive phase is quite similar to that inferred for the hard X-ray-emitting electrons, and the radio and hard X-ray light curves show similar time structure. In the radio images we can identify at least four spatially-distinct regions that show quite different temporal behaviors (Fig. 10). The brightest radio emission in the flare comes from a location to
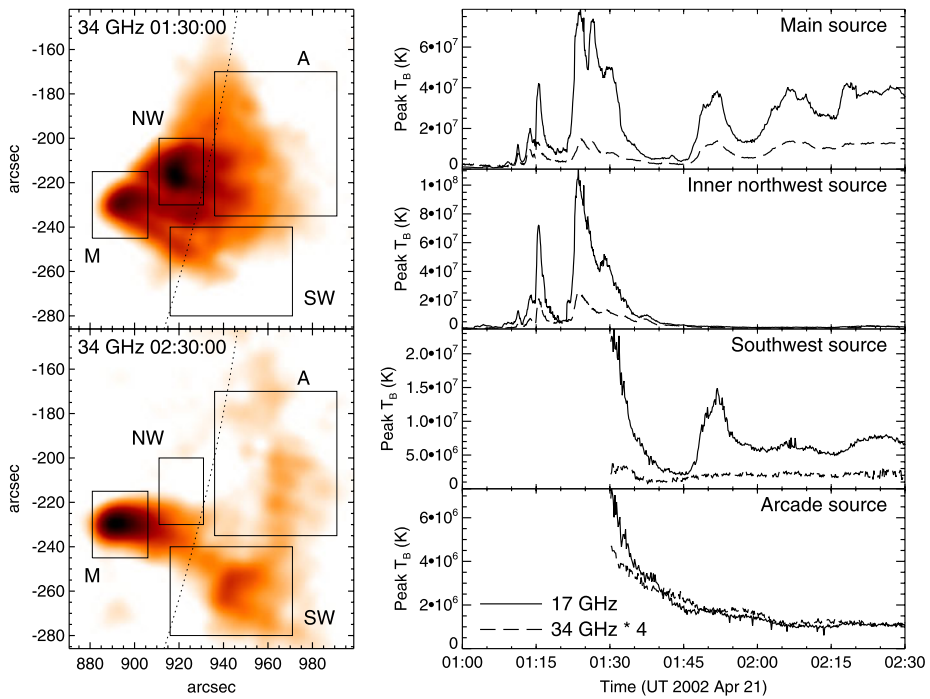
Fig. 10 Light curves for individual locations in SOL2002-04-21T01:51 (X1.5). The 34 GHz NoRH *images in the left hand panels* show the locations of the four regions chosen for investigation relative to the morphology of the source at two different times, while the *four panels on the right* show the evolution of the maximum brightness temperature in each of the regions. The light curves show both 17 and 34 GHz curves: the 34 GHz brightness temperatures are multiplied by 4, so that they should be the same as the 17 GHz values if the emission is optically-thin thermal emission (as is clearly the case for the arcade source)

the north-west of the site where the flare starts, under the middle of the loop arcade, but the radio emission from this location fades after the impulsive phase and is unimpressive during the extended decay phase. On the other hand, the main source and the thermal and non-thermal sources in the arcade (distinguishable by their brightness temperature spectra) all participate in the extended phase. This indicates that energy release is ongoing throughout this phase and apparently distributed throughout the coronal volume above the flare site.

6 Millimeter- and Submillimeter-Wavelength Emission from Flares

Radio emission from solar flares at millimeter and shorter wavelengths is expected to have two main characteristics: since optically-thin thermal emission has a flat flux spectrum, it should become increasingly important relative to the falling spectrum of nonthermal gy-rosynchrotron emission as one goes to higher frequencies. However, higher-frequency non-thermal gyrosynchrotron emission requires emission at ever higher harmonics of the electron gyrofrequency, and this makes it sensitive to electrons with much higher energies than are required for microwave emission (MeV and higher energies rather than tens to hundreds of keV: Ramaty 1969; White and Kundu 1992; Ramaty et al. 1994, and Fig. 1). Bremsstrahlung is increasingly inefficient as electron energy increases because faster electrons suffer less
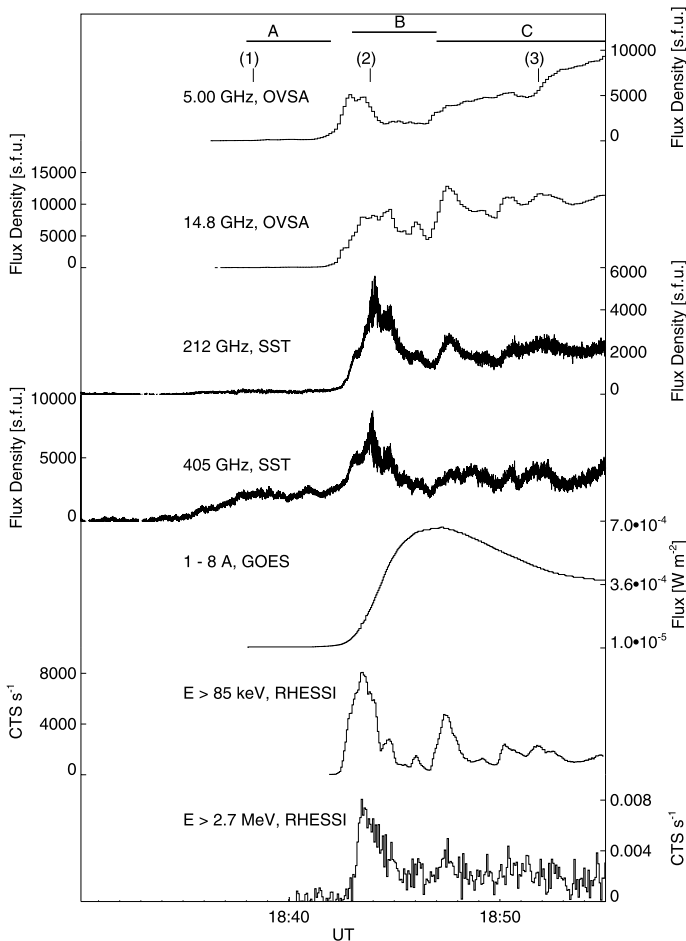
Fig. 11 Light curves for microwave, millimeter, submillimeter, hard X-ray and γ-rays from SOL2006-12-06T18:47 (X6.5) (from Kaufmann et al. 2009)

deflection by a nucleus. However, synchrotron emission increases in efficiency as electron energy increases. Thus millimeter-wavelength observations are a very sensitive diagnostic of γ-ray-emitting electrons, more sensitive, in fact, than current γ-ray detectors in the sense that nonthermal emission from smaller flares is more easily detected at millimeter wavelengths (e.g., Kundu et al. 1994; White 1994, 1999; Silva et al. 1996; Raulin et al. 1999).

During the period of *RHESSI* observations, the Solar Submillimeter Telescope (SST; Kaufmann et al. 2008) has routinely monitored the Sun at 212 and 405 GHz from the Argentinian time zone. Typically only major flares can be detected at these wavelengths, where the atmosphere has a major influence on detectability (the sky opacity at 405 GHz is generally in excess of 1).

An example of SST data is shown in Fig. 11, from SOL2006-12-06T18:47 (X6.5). This event is typical in that there is in general a good correlation between the radio emission and the HXR/γ-ray emission, consistent with the picture of the radio emission resulting

from gyrosynchrotron emission by the same nonthermal electrons that produce the HXR/γ-ray emission by bremsstrahlung. However, this event, in common with a number of others, shows a major inconsistency with this picture: the radio spectrum shows a normal nonthermal behavior with a spectral peak in the 10–20 GHz range, with a falling spectrum at high microwave frequencies, but the SST data show an increasing spectrum from 212 to 405 GHz. Such behavior is not understood. Other events detected by SST show radio spectra that are consistent with a single nonthermal electron population, as in the case described by Giménez de Castro et al. (2009): in that flare no flux was detected above 250 keV, yet the 212 GHz emission was clearly detected.

As discussed earlier, it is well known that there is generally a discrepancy between the energy distribution of the nonthermal electrons that produce the HXRs and those that produce the radio emission at high frequencies: the radio data generally show a harder spectrum (e.g., Kundu et al. 1994; Raulin et al. 1999; Silva et al. 2000). This is attributed to the fact that the energies of electrons emitting the HXRs (many tens of keV) are smaller than those of the radio-emitting electrons (hundreds of keV): if the typical electron energy spectrum breaks up at energies above a few hundred keV, this could explain the observations. In principle, γ-ray spectra should show a break up at higher photon energies if the electron energy spectrum has such a break, but in the relevant energy range (photon energies above 500 keV) it is difficult to separate the electron bremsstrahlung spectrum from the nuclear line spectrum that usually dominates γ-rays above 1 MeV. There is one class of events for which the electron bremsstrahlung spectrum above 0.5 MeV is more easily determined, the so-called "electron-dominated events" (Marschhauser et al. 1991). These events result from extremely hard electron energy spectra whose bremsstrahlung dominates the usual nuclear line region. The prototype of this class of event was SOL1989-03-06T13:56 (X15), in which the photon spectrum during the main emission peak had a spectral index of 2.5 from 0.3–0.8 MeV, flattening to about 1.4 from 1 MeV to 10 MeV (Marschhäuser et al. 1994). Petrosian et al. (1994) argued that the entire 0.3–10 MeV photon spectrum in this event can be explained by bremsstrahlung from a single electron energy distribution with power-law index 2.2. In their model, the steeper photon spectrum below 1 MeV is due to the fact that the lower-energy photons are emitted nearly isotropically whereas the higher-energy photons are preferentially beamed along the direction of electron motion into the Sun (e.g., Vestrand et al. 1987). As noted in Sect. 2.2, relativistic and electron-electron effects in a single power-law energy distribution can produce a flattening of order 0.5 in the photon spectral index above 500 keV. Trottet et al. (1998) discuss the electron-dominated flare SOL1990-06-11T09:43 (M4.5), which exhibited a flattening of the bremsstrahlung photon spectrum at high energies but also major variations in the spectrum with time. During the brightest γ-ray peak the spectrum flattened by about 1 at 700 keV, whereas during other emission peaks the lower-energy photons had a spectrum steeper by 2–2.5 than the spectrum above 400 keV. The radio spectrum from 35 to 50 GHz during the brightest peak corresponds to an electron energy distribution with index of order 3, as does the bremsstrahlung photon spectrum above the break, so in this event they appear to be compatible with a single electron energy distribution. Vilmer et al. (1999) study another electron-dominated event in which the bremsstrahlung photon spectrum flattens above 500 keV by about 1 in the spectral index.

But even a break upwards in the electron energy spectrum, as described above, cannot produce a radio spectrum that rises in the submillimeter range. One can envisage a source of ultra-relativistic leptons in a very high magnetic field region: Trottet et al. (2008) suggest that ultra-relativistic positrons resulting from pion decay are a possible source of the impulsive submillimeter component in SOL2003-10-28T11:10 (X17.2) seen in conjunction with high-energy protons (>200 MeV), although it seems unlikely that sufficient positrons can be

produced by this means and energetic electrons are still a more plausible interpretation. An optically-thick thermal source could produce a rising spectrum, but it would have to be either exceptionally large or exceptionally hot (e.g., Silva et al. 2007, who prefer an interpretation in terms of gyrosynchrotron emission from electrons in a very strong magnetic field). In the case of SOL2006-12-06T18:47 (X6.5), the SST observations place an upper limit of 15″ on the submillimeter source size, and for a source that small to produce the observed flux via thermal emission requires such high temperatures that the source would be intense in the *GOES* soft X-ray range, and would have been seen at other wavelengths (e.g., Kaufmann et al. 2009). At the time of writing, there is no completely accepted explanation for this spectral feature; a more detailed discussion of this topic may be found in Krucker et al. (2011).

7 Decimeter and Low-Frequency Radio Emission in Association with Hard X-rays

Most decimeter (300–3000 MHz) and low-frequency (here referring to frequencies below 300 MHz) emission from the Sun is dominated in flares by very bright plasma emission, i.e., conversion of electrostatic Langmuir waves at the electron plasma frequency ($f_p = 9000 n_e^{1/2}$) into electromagnetic radiation at the fundamental f_p and the second harmonic $2 f_p$. The Langmuir waves are generated by coherent processes, such as a bump-on-tail instability driven by an electron beam, and so this mechanism can reach very high brightness temperatures even though relatively few electrons are involved. Furthermore, by definition, low-frequency plasma emission comes from regions of low density, whereas hard X-ray emission by bremsstrahlung from collisions is preferentially seen from regions of high density. For this reason, we might not expect a close relationship between low-frequency radio bursts and hard X-ray emission: the electrons producing both have similar energies (plasma emission can be very strong from electrons with energies of tens of keV), but they may be located in very different environments. As an example, Vilmer et al. (2003) discuss the radio and HXR data for an M8 flare in which there are multiple HXR sources and multiple spatially-distinct radio sources in the 100–500 MHz range, but little spatial correlation between the two wavelengths: in particular the early HXR emission in the event seems to come from compact closed magnetic loops with little escape of energetic electrons onto the higher field lines where we believe that the low-frequency radio sources are located. In a later phase of this event a new HXR source low in the atmosphere is associated with the appearance of new radio sources at much greater heights, suggesting simultaneous injection of electrons over a wide range of spatial scales.

7.1 Radio Bursts and Energy Release in Flares

Benz et al. (2005) and Arzner and Benz (2005) have carried out surveys of the types of radio bursts in the range 0.1–4 GHz that occur in flares that exhibit hard X-rays, using data from the *Phoenix-2* spectrometer operated by ETH-Zürich. This frequency range is dominated by plasma emission and other forms of coherent processes such as electron cyclotron maser emission.

Benz et al. (2005) investigated 201 flares and found that about 20% of such flares did not exhibit radio emission in their range (although many of the events with no radio emission were close to the limb and that fact may play a role in their non-detection; see Benz et al. 2007), but over half of the HXR-productive flares followed a similar pattern: at lower frequencies Type III bursts (indicating electron beams) are seen propagating outwards, and at the highest frequencies the bottom of the optically-thick gyrosynchrotron continuum from

nonthermal electrons is seen, while in between (typically in the range 500 MHz to 2 GHz) pulsations and/or narrowband spikes (often attributed to electron cyclotron maser emission) may occur. Note that a plasma frequency of 1 GHz corresponds to an electron density of 1.2×10^{10} cm^{-3} and an electron cyclotron frequency of 1 GHz corresponds to a magnetic field strength of 360 G, both of which are values characteristic of the low corona and heights where we might expect energy release to be taking place, For this reason, there has long been interest in understanding the relationship between energy releases and coherent radio bursts in the decimetric range (e.g., Aschwanden et al. 1985, 1990; Güdel et al. 1991).

Arzner and Benz (2005) looked in more detail at the relationship between the timing of radio and hard X-ray emission in this frequency range. They found that only about 20% of type III bursts show a close temporal correlation with HXR peaks, generally trailing the HXR by about 0.5 seconds. Some reverse-drift and patchy bursts also show such delays relative to the HXRs. Such delays can be explained by scattering of the radio emission in the inhomogeneous medium around the source.

Narrowband decimetric spikes show the strongest association with HXRs, in the sense that 95% of such spikes occur during HXR emission (but only 2% of HXR flares show spikes; Guedel et al. 1991). The spikes have timescales shorter (<0.1 s) than we can easily measure in hard X-rays, so timing comparisons are difficult. In addition, spikes may be occurring across a range of frequencies at any given instant, so choices have to be made when making comparisons with HXR light curves. Dabrowski and Benz (2009) carry out a careful comparison of decimetric spikes and HXRs in the time domain. They cross-correlated the radio spike and *RHESSI* HXR light curves to measure delays. The mean correlation coefficient was around 0.7, which is statistically significant for the size of the sample. The delays showed a broad distribution with a standard deviation of order 4 seconds but a mean consistent with zero delay.

Battaglia and Benz (2009) investigated the relationship between spike and HXR sources by comparing the spatial locations of the two emissions for a flare at the limb. The spike locations were obtained from Nançay Radio Heliograph observations between 300 and 432 MHz, while *RHESSI* provided HXR images. The radio spikes were found to be significantly displaced from the HXR sources and at a greater height. Low-frequency radio emission is typically scattered and refracted in the corona, but any refraction will make the apparent height lower than the true height (e.g., Melrose and Dulk 1988). It is possible that there is HXR emission from the spike locations but that it is much weaker than the lower-altitude sources and is lost in the limited dynamic range of the HXR images. An occulted event would be needed to test this possibility. Ning et al. (2009) investigate some features in decimetric dynamic spectra that they argue, based on simultaneous *RHESSI* data, represent upflows due to heating of the chromosphere by nonthermal electrons.

7.2 Hard X-rays from Reverse-Drift Bursts

Electron beams are a common phenomenon in the solar corona (even in the absence of flares), visible through both their plasma emission at radio wavelengths and their bremsstrahlung hard X-ray emission if they reach the chromosphere The exact mechanism by which these electron beams are generated is still unknown. For example, X-point reconnection is believed primarily to produce oppositely directed bulk ion flows, but not collisionless electron beams, and so the production of such beams in this mechanism would require a secondary process. Detection of both radio and HXR emission from the same feature would be an important step in understanding their origin, since the HXR data reveal the energy
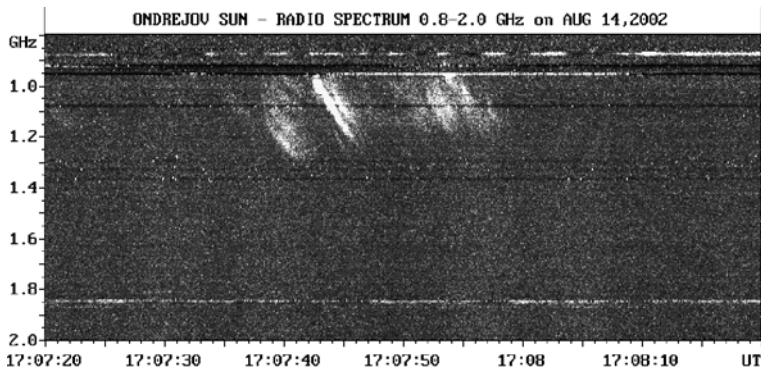
Fig. 12 A dynamic spectrum of reverse-drift radio bursts observed with the Ondrejov spectrograph between 1.0 and 1.2 GHz (Fárník and Karlický 2007)

distribution of accelerated electrons and the radio data have the potential of revealing the location of the acceleration site and the physical conditions therein.

While the most common manifestation of electron beams is the Type III radio burst (discussed next), generated by electrons moving outwards through the corona on open field lines, symmetry suggests that there should be roughly equal numbers of electron beams going downwards. If such beams generate plasma emission, they will be seen to drift from lower to higher frequencies as time proceeds, the reverse of Type III bursts, and hence they are referred to as "reverse-drift" bursts. Since the electrons in such events are moving downwards towards the chromosphere, they seem more likely to be associated with hard X-rays. At frequencies above 1 GHz, such bursts, if due to plasma emission, must arise low in the corona and propagation times down to the chromosphere are typically less than 0.5 seconds.[3]

The relationship between reverse-drift bursts and hard X-rays has been studied by Karlický et al. (2004) and Fárník and Karlický (2007). An example is shown in Fig. 12. From comparison with hard X-ray data in over 20 groups of reverse-drift bursts, these studies find that bursts are mostly observed during the rise phase of the hard X-ray emission, but in the range above 1 GHz there was no one-to-one relationship between individual HXR peaks and individual reverse-drift bursts at a time scale of order 1 second. By contrast, in the frequency range below 1.4 GHz Aschwanden et al. (1995) found correspondence between individual X-ray peaks and fast-drift radio bursts (both Type IIIs and reverse-drift bursts) at a level of 26%. Thus the higher-frequency (and presumably, higher-density environment) reverse-drift bursts above 1 GHz currently do not support the idea that such downgoing electron beams visible at radio wavelengths are responsible for the bulk of the HXRs emitted by flares.

7.3 Hard X-rays from Type III Radio Bursts

Depending on the height at which they originate, Type III radio bursts may seem to be unlikely candidates for correlation with hard X-rays. Those originating at densities below 10^9 cm^{-3} ($f_p = 300$ MHz) do not experience much column density as they travel away from

---

[3]Historical note: an early paper on flare HXR bursts by Anderson and Winckler (1962) noted the similar timing of Type III bursts and suggested that they may be due to the same electrons that produced the hard X-rays. The more likely connection to downwards-moving reverse-drift bursts, and the absence of such bursts in that event, was pointed out by Kundu (1963), with further discussion presented in Kundu (1965).

the solar surface, making it difficult for them to produce detectable bremsstrahlung HXRs as they propagate outwards. But if they have downgoing counterparts, not necessarily detected as radio sources, then the downgoing electrons will encounter a greater column density and thus could produce observable HXRs.

Type III bursts have a high degree of correlation with the onset of HXR emission in impulsive flares: in about 30% of flares (and a larger proportion of impulsive flares) Type III emission occurs as the impulsive phase begins (e.g., Cane et al. 1986; Cane and Reames 1988; Aschwanden et al. 1990), but typically these impulsive-phase radio bursts do not last for the entire period of HXR emission so a one-to-one association with HXR features cannot be established.

Saint-Hilaire et al. (2009) carry out a detailed study of the quantitative conditions needed for outward-traveling electron beams such as Type-III-emitting streams to be detectable as thin-target nonthermal HXR sources. They find that radially-extended HXR sources can indeed be produced by electron beams propagating through standard coronal density models, but only if the electron beams are intense: they find that 10^{35} electrons above 10 keV are needed for detection of the source, but that 10^{36} electrons above 10 keV are needed if *RHESSI* is to be capable of imaging the HXR source. Such strong beams are more characteristic of the downward flux at an HXR-emitting footpoint in a flare than of the outward-propagating Type-III-burst electron beams as inferred from measurements in the solar wind (Krucker et al. 2007). These calculations assume that the electron beam is generated in a region of density 3×10^9 cm^{-3} (plasma frequency of 500 MHz) in a density model with scale height $\sim 10^{10}$ cm; beams generated at lower starting densities will experience less column density and therefore will be difficult to detect unless the beams are much stronger.

Vilmer et al. (2002) compared Type III bursts with hard X-rays in one of the first flares observed by *RHESSI*, SOL2002-02-20T11:07 (C7.5). In that event the radio emission from outgoing electron beams seems to be very well correlated with hard X-ray emission. Figure 13 shows the relative locations of the HXR sources and 410 MHz emission observed with the Nançay Radio Heliograph. The *RHESSI* images show three separate sources in locations consistent with thick-target footpoint emission, each with a different temporal behavior (only two are visible in the figure). At one point there is a transition in which the source initially brightest in HXRs fades and is overtaken by a different source. This transition occurs at a time when the 410 MHz radio emission shows a distinct brightening, suggesting a causal connection between the radio and HXR emission. Nançay Radio Heliograph radio images of this event also show a transition. Initially the HXR footpoint sources occupy a spatial scale of order 20″ while the 410 MHz radio emission shows two sources

Fig. 13 *RHESSI* iso-contours (*black*) (40, 60, 80% of the maximum) at 25–40 keV and NRH contours at 410 MHz (*white*) (50, 60, 70, 80, 90%) for the SOL2002-02-20T11:07 (C7.5) (Vilmer et al. 2002). The *RHESSI* and NRH contours are superposed on an EIT image obtained at 11:12 UT
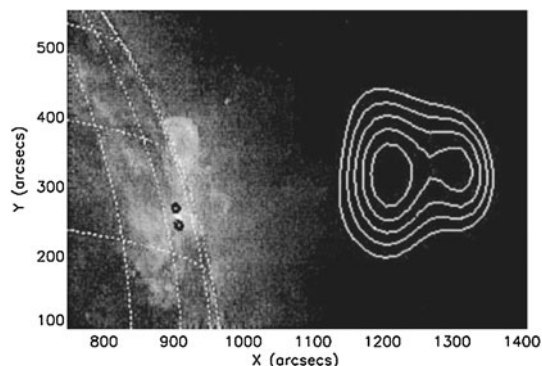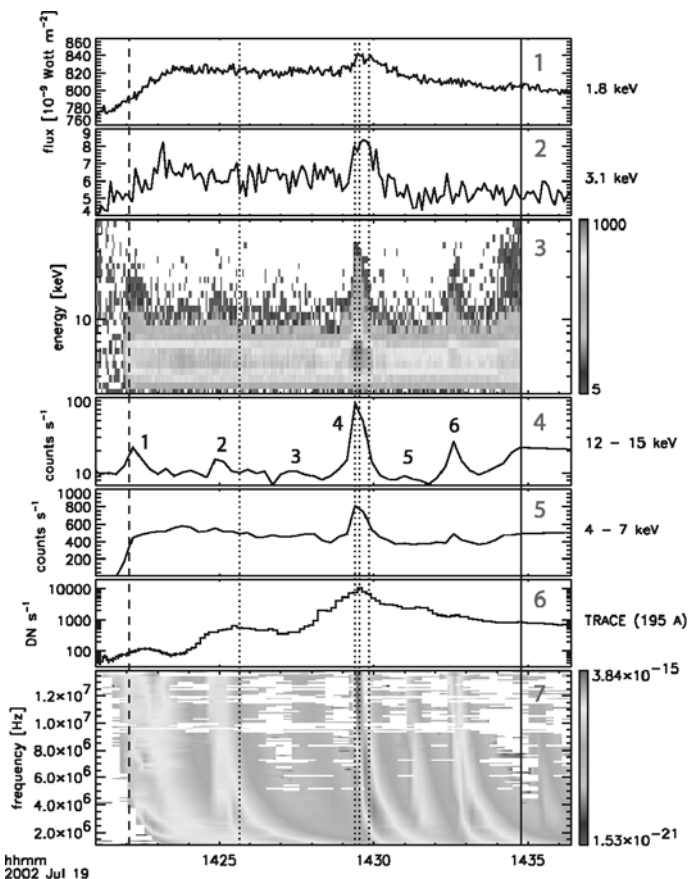
Fig. 14 Plot of a group of Type III bursts (SOL2002-07-19T14:30). *Panels 1* and *2*: *GOES* 1–8 Å (1.6 keV) and 0.5–4 Å (3.1 keV) light curves in a linear scale. *Panel 3*: *RHESSI* spectrogram plot, nighttime background-subtracted. *Panel 4*: *RHESSI* 12–15 keV light curve (nonthermal). *Panel 5*: *RHESSI* 4–7 keV light curve (thermal). *Panel 6*: *TRACE* light curve integrated over the active region from which the HXRs originated. *Panel 7*: Radio spectrogram from the *WIND/*WAVES instrument. The *dashed line* delimits the end of eclipse for *RHESSI*. The *solid line* indicates passage through the South Atlantic Anomaly during which *RHESSI* data is unavailable. From Christe et al. (2008)

aligned almost radially above the flare site at altitudes of order 300″ & 400″ above the photosphere, with the lower source being the brighter: after the transition in the location of the brightest HXR emission, the higher 410 MHz source becomes brighter. Vilmer et al. (2002) interpret the good correlation between the HXR and radio emission, which extends down to timescales as short as a few seconds, as evidence for a common acceleration site with simultaneous injection of electrons both in low-lying magnetic features where they produce hard X-rays, and in larger scale and higher magnetic structures where the radio emission is produced. Yan et al. (2006) discuss another flare in which Type III bursts are seen for a long period coincident with HXR emission, but the locations of the Type III sources are found to be a large distance from the flare site, at the edge of an associated CME, and the connection to the HXR emission is less clear.

Christe et al. (2008) investigated a group of 6 interplanetary Type III bursts that showed associated HXR emission at *RHESSI*. Figure 14 shows *RHESSI* data during a group of
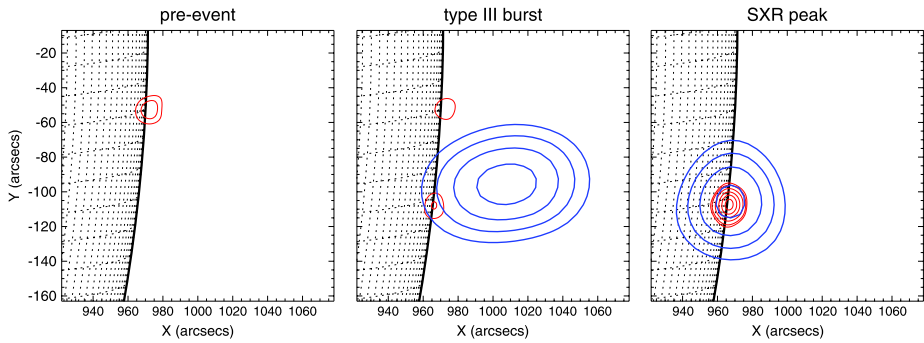
Fig. 15 *RHESSI* X-ray imaging before (*left*), during (*middle*), and after (*right*) radio Type III bursts. Thermal emission (4–8 keV) is shown in red contours (contours at 5, 10, 30, 50, 70, 90% of the level in the *final panel*) with $10''$ FWHM resolution, and the 14–30 keV emission is given in blue (levels are 65, 75, 85, and 95%) with a resolution of $60''$. From Krucker et al. (2008b)

Type III bursts observed by the *WIND*/WAVES instrument from 2–14 MHz; there is a clear correlation between the HXR peaks and the onset of Type III radio emission for this group. Christe et al. (2008) discuss (quantitatively) the possibility that the HXRs are produced by the Type III-emitting electrons via thin-target bremsstrahlung in the corona, and conclude that the number of electrons required in the Type III beam would be too large to be consistent with the observations. Instead, these events look like HXR microflares, with the HXR spectra being very soft, and the Type III bursts produced during the energy release in the same way that they are at the onset of impulsive flares. The energy releases in the events shown in Fig. 14 are less than 10^{27} erg.

On the other hand, Krucker et al. (2008b) discuss a larger event that occurred at the solar limb such that the main footpoint HXR sources are occulted and *RHESSI* could easily determine the height of the coronal HXR sources. They found that the event did show HXR sources at the solar surface, but when Type III radio emission was present there was a coronal HXR source elongated in the radial direction (see Fig. 15), consistent with expectations for thin-target HXRs from the Type III-emitting electrons. The *WIND* spacecraft was able to measure the number of nonthermal electrons in the Type III burst reaching the Earth and again it appeared to be an order of magnitude too low to explain the observed HXR flux. These quantitative comparisons are fraught with assumptions that need to be made but cannot easily be tested: for example, we must assume that *WIND* measures the bulk of the Type III electrons in the solar wind when it might be merely sampling the edge of the electron beam, and we make assumptions about the pitch-angle distribution of the nonthermal electrons in the HXR source, how long the electrons spend in the source, and how open magnetic field lines connected to the surface diverge with distance in the solar wind. These assumptions introduce uncertainties in the result, but at this point we can say that there are no cases where we can quantitatively attribute the HXR to the Type III-emitting electrons. On the other hand, based on this event we can expect that there are more cases of partially-occulted flares exhibiting radially-elongated HXR emission in conjunction with Type III bursts waiting to be identified in the *RHESSI* archive.

7.4 Acceleration Sites in the Corona

As noted above the combination of radio and HXR data is a valuable tool for understanding the location and nature of energy release sites: the radio data, in particular, identify the

density in the accelerator if radio emission at the local plasma frequency is visible. This principle has been applied by Aurass et al. (2006) in identifying a particular feature in radio dynamic spectra with the termination shock of a reconnection outflow. The argument is that reconnection sites produce bulk outflows at the Alfvén speed and these outflows are likely to terminate at a shock where the bulk flow energy in the ions can be converted into heat. Such a shock can also accelerate electrons and thus lead to observable plasma emission (Aurass et al. 2002; Aurass and Mann 2004). Figure 16 shows a slow-drift feature in the dynamic radio spectrum of SOL2003-10-28T11:10 (X17.2) that Aurass et al. (2006) interpret as such a termination shock. In this event, Nançay Radio Heliograph observations above 300 MHz (at frequencies interpreted as harmonic plasma emission) show a source at the time of the termination-shock feature that is located 0.3 R$_\odot$ (in projection onto the sky) away from the flare site (the physical distance may be larger since the flare is close to disk center; Pick et al. 2005). The radio termination-shock feature is seen at the same time that intense γ-ray emission is seen, and Aurass et al. (2006) argue that the termination shock is the acceleration site for the relativistic γ-ray-emitting electrons. Warmuth et al. (2009) and Mann et al. (2009) investigate shock-drift acceleration as a means by which the energy in such outflows may be converted into electron energy at a termination shock, utilizing the relativistic theory for shock-drift acceleration developed by Mann et al. (2006). As yet there is no independent confirmation of the presence either of reconnection outflows or a "wall" in the low-density corona suitable to terminate such a flow, so the true nature of spectral features such as that in Fig. 16 continues to be a topic for research. Additional discussion of this topic may be found in Holman et al. (2011).

This model is not alone in placing the acceleration site for very energetic electrons that produce observable HXRs and γ-rays at a considerable height such that the ambient density (in this case, with the fundamental plasma frequency being around 150 MHz in the termination shock region, the electron density is less than 3×10^8 cm^{-3}) and the magnetic field in the acceleration site are both relatively low. In such models, acceleration takes place in a relatively low-energy-density region, and then the energetic electrons must propagate a large distance back to a region of higher energy density at the flare site low in the atmosphere to produce observable bremsstrahlung. If the γ-ray sources consist of footpoints on either side of a neutral line, then presumably the oppositely-directed field lines from the active region must also thread the termination shock despite the large distance between the acceleration site and the HXR/γ-ray sources (on the other hand, non-footpoint locations for the γ-ray sources, as for the 2.223 MeV neutron-capture line, may point to an acceleration site that is not threaded by loops from the active region; Hurford et al. 2006). These complications apply to any model in which acceleration does not take place low in the corona over an active

Fig. 16 The dynamic spectrum of SOL2003-10-28T11:10 (X17.2), from the Tremsdorf spectrograph operated by the Astrophysikaliches Institut Potsdam. The bright chevron-shaped feature centered at 11:03 UT (labelled "TS") is identified as a termination-shock feature
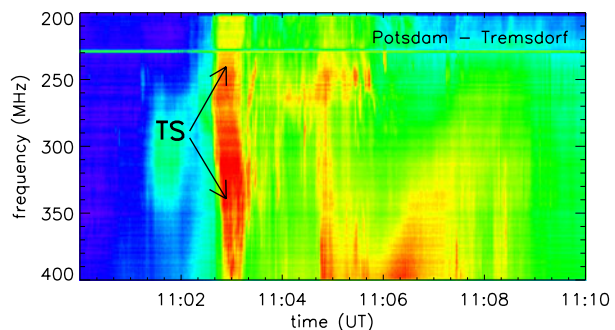
region, and distinguishing between these two classes of models remains an important step in identifying the energy release and acceleration mechanisms operating in solar flares.

8 Summary

Progress during the *RHESSI* era has confirmed the value of utilizing radio and HXR data simultaneously to study accelerated electrons in the solar corona. The complementary nature of the diagnostics in the two wavelength regimes allows one to study phenomena from differing viewpoints. However, we have not yet solved several very important problems, notably the discrepancy between the nonthermal electron energy spectral index derived from radio and HXR observations of electrons which, since they show the same temporal behavior, must be related; and the anomalous rising-spectrum submillimeter component. Both of these problems need high-frequency radio data (>30 GHz) for proper study.

References

K.A. Anderson, J.R. Winckler, J. Geophys. Res. **67**, 4103 (1962). doi:10.1029/JZ067i011p04103
K. Arzner, A.O. Benz, Sol. Phys. **231**, 117 (2005)
A. Asai, M. Shimojo, H. Isobe, T. Morimoto, T. Yokoyama, K. Shibasaki, H. Nakajima, Astrophys. J. Lett. **562**, L103 (2001)
A. Asai, H. Nakajima, M. Shimojo, S.M. White, H.S. Hudson, R.P. Lin, Publ. Astron. Soc. Jpn. **58**, L1 (2006)
A. Asai, H. Nakajima, M. Oka, K. Nishida, Y.T. Tanaka, Adv. Space Res. **39**, 1398 (2007). doi:10.1016/j.asr.2007.03.077
M. Aschwanden, A.O. Benz, S.R. Kane, Astron. Astrophys. **229**, 206 (1990)
M. Aschwanden, H.J. Wiehl, A.O. Benz, S.R. Kane, Sol. Phys. **97**, 159 (1985)
M.J. Aschwanden, A.O. Benz, B.R. Dennis, R.A. Schwartz, Astrophys. J. **455**, 347 (1995)
M.J. Aschwanden, R.A. Schwartz, Astrophys. J. **464**, 974 (1996). doi:10.1086/177385
H. Aurass, G. Mann, Astrophys. J. **615**, 526 (2004). doi:10.1086/424374
H. Aurass, K. Shibasaki, M. Reiner, M. Karlický, Astrophys. J. **567**, 610 (2002)
H. Aurass, G. Mann, G. Rausche, A. Warmuth, Astron. Astrophys. **457**, 681 (2006). doi:10.1051/0004-6361:20065238
M. Battaglia, A.O. Benz, Astron. Astrophys. **499**, L33 (2009). doi:10.1051/0004-6361/200912143
A.O. Benz, P.C. Grigis, A. Csillaghy, P. Saint-Hilaire, Sol. Phys. **226**, 121 (2005)
A.O. Benz, R. Brajša, J. Magdalenić, Sol. Phys. **240**, 240 (2007)
L. Bone, J.C. Brown, L. Fletcher, A. Veronig, S. White, Astron. Astrophys. **466**, 339 (2007)
J.C. Brown, Sol. Phys. **18**, 489 (1971)
J.C. Brown, M.J. Aschwanden, E.P. Kontar, Sol. Phys. **210**, 373 (2002). doi:10.1023/A:1022469402781
H.V. Cane, D.V. Reames, Astrophys. J. **325**, 895 (1988)
H.V. Cane, R.E. McGuire, T.T. von Rosenvinge, Astrophys. J. **301**, 448 (1986). doi:10.1086/163913
A. Caspi, Ph.D. Dissertation, U.C. Berkeley, 2010
A. Caspi, R.P. Lin, Astrophys. J. Lett. **725**, L161 (2010). doi:10.1088/2041-8205/725/2/L161
S. Christe, S. Krucker, R.P. Lin, Astrophys. J. Lett. **680**, L149 (2008). doi:10.1086/589971
B.P. Dabrowski, A.O. Benz, Astron. Astrophys. **504**, 565 (2009). doi:10.1051/0004-6361/200811108
C. Dauphin, N. Vilmer, T. Lüthi, G. Trottet, S. Krucker, A. Magun, Adv. Space Res. **35**, 1805 (2005)
C. Dauphin, N. Vilmer, S. Krucker, Astron. Astrophys. **455**, 339 (2006)

G.A. Dulk, Annu. Rev. Astron. Astrophys. **23**, 169 (1985)

G.A. Dulk, K.A. Marsh, Astrophys. J. **259**, 350 (1982)

F. Fárník, M. Karlický, Sol. Phys. **240**, 121 (2007). doi:10.1007/s11207-006-0238-7

G.D. Fleishman, A.A. Kuznetsov, Astrophys. J. **721**, 1127 (2010). doi:10.1088/0004-637X/721/2/1127

G.D. Fleishman, V.F. Melnikov, Astrophys. J. **587**, 823 (2003a)

G.D. Fleishman, V.F. Melnikov, Astrophys. J. **593**, 598 (2003b)

G.D. Fleishman, T.S. Bastian, D.E. Gary, Astrophys. J. **684**, 1433 (2008). doi:10.1086/589821

L. Fletcher, B.R. Dennis, H.S. Hudson, S. Krucker, A. Veronig, M. Battaglia, L. Bone, Q. Chen, P. Gallagher, P.T. Grigis, H. Ji, W. Liu, R.O. Milligan, M. Temmer, Space Sci. Rev. (2011, this issue)

K.J. Frost, B.R. Dennis, Astrophys. J. **165**, 655 (1971)

C.G. Giménez de Castro, G. Trottet, A. Silva-Valio, S. Krucker, J.E.R. Costa, P. Kaufmann, E. Correia, H. Levato, Astron. Astrophys. **507**, 433 (2009). doi:10.1051/0004-6361/200912028

V.V. Grechnev, S.M. White, M.R. Kundu, Astrophys. J. **588**, 1163 (2003)

M. Güdel, M. Aschwanden, A.O. Benz, Astron. Astrophys. **251**, 285 (1991)

M. Guedel, A.O. Benz, M.J. Aschwanden, Astron. Astrophys. **251**, 285 (1991)

D.A. Guidice, J.P. Castelli, Sol. Phys. **44**, 155 (1975)

I.G. Hannah, H.S. Hudson, M. Battaglia, S. Christe, J. Kašparová, M. Kundu, S. Krucker, A. Veronig, Space Sci. Rev. (2011)

G.D. Holman, L. Sui, R.A. Schwartz, A.G. Emslie, Astrophys. J. Lett. **595**, L97 (2003)

G.D. Holman, M.J. Aschwanden, H. Aurass, M. Battaglia, P. Grigis, E.P. Kontar, W. Liu, P. Saint-Hilaire, V.V. Zharkova, Space Sci. Rev. (2011, this issue)

H.S. Hudson, R.C. Canfield, S.R. Kane, Sol. Phys. **60**, 137 (1978)

G.J. Hurford, S. Krucker, R.P. Lin, R.A. Schwartz, G.H. Share, D.M. Smith, Astrophys. J. Lett. **644**, L93 (2006). doi:10.1086/505329

S.R. Kane, K.A. Anderson, W.D. Evans, R.W. Klebesadel, J. Laros, Astrophys. J. Lett. **233**, L151 (1979). doi:10.1086/183095

M. Karlický, New Astron. **9**, 383 (2004). doi:10.1016/j.newast.2004.01.002

M. Karlický, F. Fárník, S. Krucker, Astron. Astrophys. **419**, 365 (2004). doi:10.1051/0004-6361:20035817

P. Kaufmann, H. Levato, M.M. Cassiano, E. Correia, J.E.R. Costa, C.G. Giménez de Castro, R. Godoy, R.K. Kingsley, J.S. Kingsley, A.S. Kudaka, R. Marcon, R. Martin, A. Marun, A.M. Melo, P. Pereyra, J. Raulin, T. Rose, A. Silva Valio, A. Walber, P. Wallace, A. Yakubovich, M.B. Zakia, in *Society of Photo-Optical Instrumentation Engineers (SPIE) Conference Series*, vol. 7012 (2008). doi:10.1117/12.788889

P. Kaufmann, G. Trottet, C.G. Giménez de Castro, J.-P. Raulin, S. Krucker, A.Y. Shih, H. Levato, Sol. Phys. **255**, 131 (2009). doi:10.1007/s11207-008-9312-7

K.-L. Klein, Astron. Astrophys. **183**, 341 (1987)

E.P. Kontar, J.C. Brown, A.G. Emslie, W. Hajdas, G.D. Holman, G.J. Hurford, J. Kašparová, P.C.V. Mallik, A.M. Massone, M.L. McConnell, M. Piana, M. Prato, E.J. Schmahl, E. Suarez-Garcia, Space Sci. Rev. (2011, this issue)

T. Kosugi, B.R. Dennis, K. Kai, Astrophys. J. **324**, 1118 (1988)

S. Krucker, E.P. Kontar, S. Christe, R.P. Lin, Astrophys. J. Lett. **663**, L109 (2007). doi:10.1086/519373

S. Krucker, M. Battaglia, P.J. Cargill, L. Fletcher, H.S. Hudson, A.L. MacKinnon, S. Masuda, L. Sui, M. Tomczak, A.L. Veronig, L. Vlahos, S.M. White, Astron. Astrophys. Rev. **16**, 155 (2008a)

S. Krucker, P. Saint-Hilaire, S. Christe, S.M. White, A.D. Chavier, S.D. Bale, R.P. Lin, Astrophys. J. **681**, 644 (2008b). doi:10.1086/588549

S. Krucker, H.S. Hudson, L. Glesener, S.M. White, S. Masuda, J.-P. Wuelser, R.P. Lin, Astrophys. J. **714**, 1108 (2010). doi:10.1088/0004-637X/714/2/1108

S. Krucker, T.S. Bastian, C.G. Gimenéz de Castro, A.S. Hales, H.S. Hudson, J. Kašparová, K.-L. Klein, M. Kretzschmar, T. Lüthi, A.L. MacKinnon, S. Pohjolainen, G. Trottet, S.M. White, Space Sci. Rev. (2011, in preparation)

M.R. Kundu, J. Geophys. Res. **66**, 4308 (1961)

M.R. Kundu, Space Sci. Rev. **2**, 438 (1963). doi:10.1007/BF00173952

M.R. Kundu, *Solar Radio Astronomy* (Interscience, New York, 1965)

M.R. Kundu, S.M. White, N. Gopalswamy, J. Lim, Astrophys. J. Suppl. Ser. **90**, 599 (1994)

M.R. Kundu, V.I. Garaimov, S.M. White, S. Krucker, Astrophys. J. **600**, 1052 (2004). doi:10.1086/379876

M.R. Kundu, E.J. Schmahl, P.C. Grigis, V.I. Garaimov, K. Shibasaki, Astron. Astrophys. **451**, 691 (2006). doi:10.1051/0004-6361:20053987

M.R. Kundu, V.V. Grechnev, S.M. White, E.J. Schmahl, N.S. Meshalkina, L.K. Kashapova, Sol. Phys. **260**, 135 (2009). doi:10.1007/s11207-009-9437-3

Y.P. Li, W.Q. Gan, Astrophys. J. Lett. **629**, L137 (2005). doi:10.1086/444617

G. Mann, H. Aurass, A. Warmuth, Astron. Astrophys. **454**, 969 (2006). doi:10.1051/0004-6361:20064990

G. Mann, A. Warmuth, H. Aurass, Astron. Astrophys. **494**, 669 (2009). doi:10.1051/0004-6361:200810099

H. Marschhauser, E. Rieger, G. Kanbach, in *International Cosmic Ray Conference*, vol. 3 (1991), p. 61

H. Marschhäuser, E. Rieger, G. Kanbach, in *High-Energy Solar Phenomena—A New Era of Spacecraft Measurements*, ed. by J. Ryan, W.T. Vestrand. American Institute of Physics Conference Series, vol. 294 (1994), pp. 171–176. doi:10.1063/1.45186

S. Masuda, T. Kosugi, H. Hara, S. Tsuneta, Y. Ogawara, Nature **371**, 495 (1994)

D.L. McKenzie, Sol. Phys. **40**, 183 (1975)

J.M. McTiernan, V. Petrosian, Astrophys. J. **359**, 541 (1990). doi:10.1086/169085

V.F. Melnikov, in *Solar Physics with the Nobeyama Radioheliograph* (2006), pp. 11–22

V.F. Melnikov, V.E. Reznikova, S.P. Gorbikov, K. Shibasaki, in *Recent Advances in Astronomy and Astrophysics*, ed. by N. Solomos. American Institute of Physics Conference Series, vol. 848 (2006), pp. 123–132. doi:10.1063/1.2347968

D.B. Melrose, G.A. Dulk, Sol. Phys. **116**, 141 (1988)

T. Minoshima, T. Yokoyama, N. Mitani, Astrophys. J. **673**, 598 (2008). doi:10.1086/523884

H. Nakajima, T. Kosugi, K. Kai, S. Enome, Nature **305**, 292 (1983)

V.M. Nakariakov, V.F. Melnikov, Astron. Astrophys. **446**, 1151 (2006). doi:10.1051/0004-6361:20053944

V.M. Nakariakov, E. Verwichte, Living Rev. Sol. Phys. **2**, 3 (2005)

Z. Ning, Astrophys. J. Lett. **671**, L197 (2007). doi:10.1086/525249

Z. Ning, Sol. Phys. **247**, 53 (2008a). doi:10.1007/s11207-007-9101-8

Z. Ning, Astrophys. J. **686**, 674 (2008b). doi:10.1086/590652

Z. Ning, W. Cao, Sol. Phys. **257**, 335 (2009). doi:10.1007/s11207-009-9388-8

Z. Ning, W. Cao, J. Huang, G. Huang, Y. Yan, H. Feng, Astrophys. J. **699**, 15 (2009). doi:10.1088/0004-637X/699/1/15

N. Nitta, S.M. White, E.J. Schmahl, M.R. Kundu, Sol. Phys. **132**, 125 (1991)

L.E. Peterson, J.R. Winckler, Phys. Rev. Lett. **1**, 205 (1958)

V. Petrosian, Astrophys. J. **251**, 727 (1981). doi:10.1086/159517

V. Petrosian, Astrophys. J. Lett. **255**, L85 (1982)

V. Petrosian, J.M. McTiernan, H. Marschhauser, Astrophys. J. **434**, 747 (1994)

M. Pick, J.-M. Malherbe, A. Kerdraon, D.J.F. Maia, Astrophys. J. **631**, L97 (2005)

J. Qiu, C. Liu, D.E. Gary, G.M. Nita, H. Wang, Astrophys. J. **612**, 530 (2004). doi:10.1086/422401

R. Ramaty, Astrophys. J. **158**, 753 (1969)

R. Ramaty, R.A. Schwartz, S. Enome, H. Nakajima, Astrophys. J. **436**, 941 (1994)

J. Raulin, S.M. White, M.R. Kundu, A.R. Silva, K. Shibasaki, Astrophys. J. **522**, 547 (1999)

J.-P. Raulin, V.S. Makhmutov, P. Kaufmann, A.A. Pacini, T. Lüthi, H.S. Hudson, D.E. Gary, Sol. Phys. **223**, 181 (2004)

V.E. Reznikova, V.F. Melnikov, K. Shibasaki, S.P. Gorbikov, N.P. Pyatakov, I.N. Myagkova, H. Ji, Astrophys. J. **697**, 735 (2009). doi:10.1088/0004-637X/697/1/735

R.D. Robinson, in *Solar Radiophysics* (Cambridge University Press, Cambridge, 1985), p. 385

P. Romano, F. Zuccarello, L. Fletcher, F. Rubio da Costa, H.M. Bain, L. Contarino, Astron. Astrophys. **498**, 901 (2009). doi:10.1051/0004-6361/200811309

P. Saint-Hilaire, S. Krucker, S. Christe, R.P. Lin, Astrophys. J. **696**, 941 (2009). doi:10.1088/0004-637X/696/1/941

A.V.L. Silva, S.M. White, R.P. Lin, I. de Pater, K. Shibasaki, H.S. Hudson, M.R. Kundu, Astrophys. J. Lett. **458**, L49 (1996)

A.V.R. Silva, H. Wang, D.E. Gary, Astrophys. J. **545**, 1116 (2000)

A.V.R. Silva, G.H. Share, R.J. Murphy, J.E.R. Costa, C.G. Giménez de Castro, J.-P. Raulin, P. Kaufmann, Sol. Phys. **245**, 311 (2007). doi:10.1007/s11207-007-9044-0

D.M. Smith, G.H. Share, R.J. Murphy, R.A. Schwartz, A.Y. Shih, R.P. Lin, Astrophys. J. Lett. **595**, L81 (2003)

T. Takakura, Sol. Phys. **26**, 151 (1972)

G. Trottet, N. Vilmer, C. Barat, A. Benz, A. Magun, A. Kuznetsov, R. Sunyaev, O. Terekhov, Astron. Astrophys. **334**, 1099 (1998)

G. Trottet, S. Krucker, T. Lüthi, A. Magun, Astrophys. J. **678**, 509 (2008). doi:10.1086/528787

V. Tzatzakis, A. Nindos, C.E. Alissandrakis, Sol. Phys. **253**, 79 (2008). doi:10.1007/s11207-008-9263-z

A.M. Veronig, J.C. Brown, Astrophys. J. Lett. **603**, L117 (2005)

W.T. Vestrand, Sol. Phys. **118**, 95 (1988)

W.T. Vestrand, D.J. Forrest, E.L. Chupp, E. Rieger, G.H. Share, Astrophys. J. **322**, 1010 (1987)

N. Vilmer, G. Trottet, C. Barat, R.A. Schwartz, S. Enome, A. Kuznetsov, R. Sunyaev, O. Terekhov, Astron. Astrophys. **342**, 575 (1999)

N. Vilmer, S. Krucker, R.P. Lin, the *RHESSI* Team. Sol. Phys. **210**, 261 (2002)

N. Vilmer, S. Krucker, G. Trottet, R.P. Lin, Adv. Space Res. **32**, 2509 (2003). doi:10.1016/S0273-1177(03)90423-6

A. Warmuth, G. Mann, H. Aurass, Astron. Astrophys. **494**, 677 (2009). doi:10.1051/0004-6361:200810101

S.M. White, in *High Energy Solar Phenomena: A New Era of Spacecraft Measurements*, vol. 294, ed. by J. Ryan, W.T. Vestrand (American Institute of Physics, New York, 1994), p. 199

S.M. White, in *Nobeyama Symposium on Solar Physics with Radio Observations*, ed. by T.S. Bastian, N. Gopalswamy, K. Shibasaki (Nobeyama Radio Observatory, Nobeyama, 1999), p. 223

S.M. White, M.R. Kundu, Sol. Phys. **141**, 347 (1992)

S.M. White, S. Krucker, K. Shibasaki, T. Yokoyama, M. Shimojo, M.R. Kundu, Astrophys. J. Lett. **595**, 111 (2003)

S.M. White, R.J. Thomas, R.A. Schwartz, Sol. Phys. **227**, 231 (2005)

Y. Yan, M. Pick, M. Wang, S. Krucker, A. Vourlidas, Sol. Phys. **239**, 277 (2006). doi:10.1007/s11207-006-0202-6